ATLAS NOTE

ATLAS-CONF-2013-070

July 15, 2013

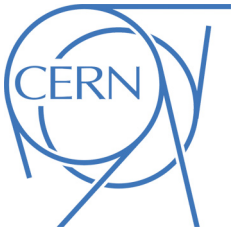

Search for New Phenomena in Events with Three Charged Leptons at $\sqrt{s} = 8$ TeV with the ATLAS detector

The ATLAS Collaboration

Abstract

A generic search for anomalous production of events with at least three charged leptons is presented. The search uses a pp-collision data sample at a center-of-mass energy of $\sqrt{s} =$ 8 TeV corresponding to 20.3 fb^{-1} of integrated luminosity collected in 2012 by the ATLAS detector at the Large Hadron Collider. Events are required to contain at least two electrons or muons, or one of each, while the third lepton may either be an additional electron or muon, or a hadronically decaying tau lepton. No significant excess above backgrounds expected from Standard Model processes is observed. Results are presented as upper limits on event yields from non-Standard-Model processes producing at least three prompt, isolated leptons, given as functions of lower bounds on several kinematic variables. Fiducial efficiencies for model testing are also provided.

ATLAS-CONF-2013-070
18 July 2013

1 Introduction

Events with more than two energetic, prompt, and isolated charged leptons are rarely produced at hadron colliders. Such events offer a clean probe of electroweak processes at high center-of-mass energies, and their production at enhanced rates above Standard Model predictions would constitute evidence for new phenomena. Models predicting events with multiple leptons in the final state include excited neutrino models [1, 2], fourth-generation quark models [3], the Zee–Babu neutrino mass model [4–6], supersymmetry [7–15], and models with doubly-charged Higgs bosons [16, 17], including Higgs triplet models [18, 19]. The production of such multilepton events in the Standard Model is dominated by WZ and ZZ production, where both bosons decay leptonically. Smaller contributions come from events with top-quark pairs produced in association with a W or Z boson, and from triboson production. Prompt leptons are those produced directly in the decay of W or Z bosons, τ leptons, or new particles that decay to leptons. Isolated but non-prompt lepton candidates misidentified as prompt arise in Drell–Yan events produced in association with a photon that converts in the detector and is reconstructed as an electron. Prompt but non-isolated leptons misidentified as isolated can arise from Dalitz decays [20, 21]. Additional non-prompt, non-isolated leptons arise from heavy-flavor decays and from mesons that decay in flight. Fake leptons can arise from hadrons that satisfy the lepton identification criteria.

This note presents a search for the anomalous production of events with at least three charged leptons in the final state. The search uses a data set collected in 2012 by the ATLAS detector at the CERN Large Hadron Collider corresponding to 20.3 fb^{-1} of pp collisions at a center-of-mass energy of $\sqrt{s} = 8$ TeV. This search follows the methodology presented in a previous ATLAS search [22]. Events are required to have at least two isolated electrons or muons, or one of each, while the third lepton may be either an additional electron or muon or a hadronically decaying tau lepton (τ_{had}).

Selected events are grouped into four categories by the presence or absence of a τ_{had} candidate and by the presence or absence of a combination of leptons consistent with a Z-boson decay. The search is carried out separately in each category by inspecting several variables of interest. The results of the search are presented as model-independent limits. Efficiencies for selecting leptons within the fiducial volume are also presented in order to aid the interpretation of the results in the context of specific models of new phenomena.

Related searches for new phenomena in events with multilepton final states have not shown any significant deviation from Standard Model expectations. The CMS Collaboration has conducted a search similar to the one presented here using 4.98 fb^{-1} of 7 TeV data [23]. The ATLAS Collaboration has performed a search for supersymmetry in final states with three leptons [24–26], as have experiments at the Tevatron [27, 28]. The search presented here complements the previous searches by providing limits outside of the context of a specific model of new phenomena.

This note is organized as follows: the ATLAS detector is described in Section 2, followed by a description of the samples and event selection in Sections 3 and 4, respectively. The categorization of events and definition of signal regions is presented in Section 5. The background estimation techniques and the results of the application of those techniques in control regions are described in Section 6. Systematic uncertainties are discussed in Section 7. The results of the search are presented in Section 8. Fiducial efficiencies for model testing are provided in Section 9.

2 The ATLAS detector

The ATLAS experiment [29] is a multipurpose particle physics detector with a forward-backward symmetric cylindrical geometry and nearly 4π coverage in solid angle [1]. The inner tracking detector covers

[1] ATLAS uses a right-handed coordinate system with its origin at the nominal interaction point (IP) in the center of the detector and the z-axis along the beam pipe. The x-axis points from the IP to the center of the LHC ring, and the y-axis points

the pseudorapidity range $|\eta| < 2.5$, and consists of a silicon pixel detector, a silicon microstrip detector (SCT), and for $|\eta| < 2.0$, a straw tube transition radiation tracker. The inner detector is surrounded by a thin superconducting solenoid providing a 2 T magnetic field. The calorimeter system covers the pseudorapidity range $|\eta| < 4.9$. Within the region $|\eta| < 3.2$, electromagnetic calorimetry is provided by barrel and end-cap high-granularity lead liquid-argon (LAr) electromagnetic calorimeters, with an additional thin LAr presampler covering $|\eta| < 1.8$, to correct for energy loss in material upstream of the calorimeters. Hadronic calorimetry is provided by a steel/scintillating-tile calorimeter, segmented into three barrel structures within $|\eta| < 1.7$, and two copper/LAr hadronic endcap calorimeters. The solid angle coverage is completed with forward copper/LAr and tungsten/LAr calorimeter modules optimised for electromagnetic and hadronic measurements respectively. The muon spectrometer surrounds the calorimeters. It consists of three large air-core superconducting toroid systems with eight coils each and stations of precision tracking and trigger chambers providing accurate muon tracking for $|\eta| < 2.7$. A three-level trigger system [30] is used to select events for further analysis offline.

3 Monte Carlo simulation and data sets

Monte Carlo (MC) simulation samples are used to estimate backgrounds from events with three prompt leptons. The ATLAS detector is simulated using GEANT4 [31], and simulated [32] events are reconstructed using the same software as that used for collision data. Small post-reconstruction corrections are applied to account for differences in efficiency, momentum resolution and scale, and energy resolution and scale between data and simulation [33, 34].

The largest Standard Model backgrounds with at least three prompt leptons are WZ and ZZ production where the bosons decay leptonically. These processes are modeled with SHERPA 1.4.1 [35]. These samples include the case where the Z boson (or γ^*) is off-shell, and the γ^* has an invariant mass above twice the muon (tau) mass for $\gamma^* \to \mu\mu$ ($\gamma^* \to \tau\tau$), and above 100 MeV for $\gamma^* \to ee$. Diagrams where a γ^* is produced as radiation from a final-state lepton and decays to additional leptons, *i.e.* $W \to \ell^*\nu \to \ell\gamma^*\nu \to \ell\ell'\ell'\nu$ and $Z \to \ell\ell^* \to \ell\ell\gamma^* \to \ell\ell\ell'\ell'$, where ℓ and ℓ' need not have the same flavor, are also included. The leading-order predictions from SHERPA are cross-checked with next-to-leading-order calculations from POWHEG 1.0 [36]. Diagrams including a Standard Model Higgs boson have negligible contributions in all signal regions under study.

The production of $t\bar{t}+W/Z$ processes (also denoted $t\bar{t}+V$) is simulated with MADGRAPH 5.1.3.28 [37] for the matrix element and PYTHIA 6.425 [38] for the parton shower and fragmentation. Corrections to the normalization from higher-order effects for these samples are 30% [39, 40]. Leptons from Drell–Yan processes produced in association with a photon that converts in the detector (denoted $Z+\gamma$ in the following) are modeled with PYTHIA. Additional samples are used to model dilepton backgrounds for control regions with fewer than three leptons. Events from $t\bar{t}$ production are generated using POWHEG with PYTHIA used for the parton shower and fragmentation. Events from Z+jets, W+jets and $W+\gamma$ production are simulated with ALPGEN 2.13 [41] for the matrix element, HERWIG 6.520 [42] for the parton shower and fragmentation, and JIMMY 4.31 [43] for the underlying event.

The parton distribution functions (PDF) for the SHERPA and POWHEG samples are taken from CT10 [44], and from MRST2007 LO** [45] for the PYTHIA and HERWIG samples. For the POWHEG $t\bar{t}$ sample, and the MADGRAPH and ALPGEN samples, the CTEQ6L1 [46] PDF is used. The MC@NLO sample uses CTEQ6.6 [47].

Additional pp interactions (pileup) in the same or nearby bunch crossings are modeled with PYTHIA. Simulated events are reweighted to reproduce the distribution of pp interactions per crossing observed in data over the course of the 2012 run. The uncertainty on the luminosity is 2.8% and is derived, following

upward. Cylindrical coordinates (r, ϕ) are used in the transverse plane, ϕ being the azimuthal angle around the beam pipe. The pseudorapidity is defined in terms of the polar angle θ as $\eta = -\ln\tan(\theta/2)$. The variable ΔR is used to evaluate the distance between objects, and is defined as: $\Delta R = \sqrt{(\Delta\phi)^2 + (\Delta\eta)^2}$.

the same methodology as that detailed in Ref. [48], from a preliminary calibration of the luminosity scale obtained from beam-separation scans performed in November 2012.

4 Event Selection

Events are required to have triggered either the single-electron or the single-muon trigger. The electron and muon triggers require a minimum threshold on the momentum transverse to the beamline (p_{T}) of 24 GeV along with an isolation requirement on the lepton. The electron trigger is complemented by a single-electron trigger with no isolation requirement with a threshold at 60 GeV. The muon trigger is complemented by a single-muon trigger with no isolation with a threshold at 36 GeV. The efficiency of the trigger requirements for events satisfying all selection criteria is typically above 90%. In order to ensure that the efficiency is independent of the p_{T} of the leptons, the offline event selection requires that at least one lepton (electron or muon) has $p_{\mathrm{T}} \geq 26$ GeV. At least one such lepton must also be consistent with having triggered the relevant single-lepton trigger. A muon associated with the trigger must lie within $|\eta| < 2.4$ due to the limited acceptance of the muon trigger, while triggered electrons must lie within $|\eta| < 2.47$, excluding the calorimeter barrel/end-cap transition region ($1.37 \leq |\eta| < 1.52$). Additional muons in the event must lie within $|\eta| < 2.5$ and have $p_{\mathrm{T}} \geq 15$ GeV. Additional electrons must satisfy the same η requirements as triggered electrons, and must have $p_{\mathrm{T}} \geq 15$ GeV. The third lepton in the event may be an additional electron or muon satisfying the same requirements as the second lepton, or a τ_{had} with $p_{\mathrm{T}}^{\mathrm{vis}} \geq 20$ GeV and $|\eta^{\mathrm{vis}}| < 2.5$, where $p_{\mathrm{T}}^{\mathrm{vis}}$ and η^{vis} denote the p_{T} and η of the visible products of the tau decay, with no corrections for the momentum carried by neutrinos. Throughout this note the four-momenta of tau candidates are defined only by the visible decay products.

All parts of the detector are required to have been operating properly for the events under study. Events must have a reconstructed primary vertex candidate with at least three associated tracks, where each track must have $p_{\mathrm{T}} > 0.4$ GeV. In events with multiple primary vertex candidates, the primary vertex is chosen to be the one with the largest value of Σp_{T}^2, where the sum is taken over all reconstructed tracks associated with the vertex. Events with pairs of leptons that are of the same flavor but opposite sign and have an invariant mass below 15 GeV are excluded to avoid contributions from low-mass hadronic resonances.

The lepton selection includes requirements to reduce the contributions from non-prompt or fake lepton candidates. These requirements exploit the transverse and longitudinal impact parameters of their tracks with respect to the primary vertex, the isolation of the lepton candidates from nearby hadronic activity, and in the case of electron and τ_{had} candidates, the lateral and longitudinal profiles of the shower in the electromagnetic calorimeter. There are also requirements for electrons on the quality of the reconstructed track and its match to the cluster in the calorimeter. These requirements are described in more detail below.

Electron candidates are required to satisfy the "tight" identification criteria described in Ref. [33], updated for the increased pileup in the 2012 data set. Muons must have tracks with hits in both the inner tracking detector and muon spectrometer, and must satisfy criteria on track quality described in Ref. [34].

The transverse impact parameter significance is defined as $|d_0/\sigma(d_0)|$, where d_0 is the transverse impact parameter of the reconstructed track with respect to the primary vertex and $\sigma(d_0)$ is the estimated uncertainty on d_0. This quantity must be less than 3.0 for electron and muon candidates. The longitudinal impact parameter z_0 must satisfy $|z_0 \sin(\theta)| < 0.5$ mm for both electrons and muons.

Electrons and muons are required to be isolated through the use of two variables sensitive to the amount of hadronic activity near the candidate. The first, $p_{\mathrm{T,track}}^{\mathrm{iso}}$, is the scalar sum of the transverse momenta of all tracks with $p_{\mathrm{T}} \geq 1$ GeV in a cone of $\Delta R < 0.3$ around the lepton axis. The sum excludes the track associated with the lepton candidate, and also excludes tracks inconsistent with originating from the primary vertex. The second, $E_{\mathrm{T,cal}}^{\mathrm{iso}}$, is the sum of the transverse energies of cells in

the electromagnetic and hadronic calorimeters in a cone of the same size. For electron candidates this sum excludes a rectangular region around the candidate axis of 0.125×0.172 in $\eta \times \phi$ (corresponding to 5×7 cells in the main sampling layer of the electromagnetic calorimeter) and is corrected for the imperfect containment of the electron transverse energy within the excluded region. For muons, the sum only includes cells above a certain threshold in order to suppress noise, and does not include cells with energy deposits from the muon candidate. For both electrons and muons, the value of $E_{\mathrm{T,cal}}^{\mathrm{iso}}$ is corrected for the expected effects of pileup interactions. Electron and muon candidates are required to have $p_{\mathrm{T,track}}^{\mathrm{iso}}/p_{\mathrm{T}} < 0.1$ and $E_{\mathrm{T,cal}}^{\mathrm{iso}}/p_{\mathrm{T}} < 0.1$. The isolation requirements for muon candidates with $p_{\mathrm{T}} > 100\,\mathrm{GeV}$ are relaxed; the muon candidates with $p_{\mathrm{T}} > 100\,\mathrm{GeV}$ must satisfy $p_{\mathrm{T,track}}^{\mathrm{iso}} < (10\,\mathrm{GeV} + 0.01\,p_{\mathrm{T}})$ and $E_{\mathrm{T,cal}}^{\mathrm{iso}} < (10\,\mathrm{GeV} + 0.01\,p_{\mathrm{T}})$.

Jets in the event are reconstructed using the FastJet [49] implementation of the anti-k_t algorithm [50], with distance parameter $R = 0.4$. The jet four-momenta are corrected for the non-compensating nature of the calorimeter, for inactive material in front of the calorimeters, and for pileup [51, 52]. Jets used in this analysis are required to have $p_{\mathrm{T}} \geq 30\,\mathrm{GeV}$ and lie within $|\eta| < 4.9$. Jets within the acceptance of the inner tracking detector must fulfill a requirement, based on tracking information, that they originate from the primary vertex. Jets containing b-hadron decays are identified using a multivariate technique [53] based on quantities such as the impact parameters of the tracks associated with the jet. The 85%-efficient working point [54] of the identification algorithm is used and jets passing the selection are referred to as b-tags. The missing transverse momentum is defined as the negative vector sum of the transverse momenta of reconstructed jets, leptons, and any remaining calorimeter clusters unassociated with reconstructed objects. The magnitude of the missing transverse momentum is denoted $E_{\mathrm{T}}^{\mathrm{miss}}$.

Tau leptons decaying to an electron (muon) and neutrinos are selected with the nominal identification criteria described above, and are classified as electrons (muons). Hadronically decaying tau candidates are constructed from jet candidates and are then selected using a projective likelihood function (LLH) identification algorithm, which is trained to distinguish hadronically decaying tau leptons from quark- and gluon-initiated jets [55]. The LLH is trained separately for tau candidates with one and three charged decay products, referred to as "one-prong" and "three-prong" taus, respectively. In this analysis, only one-prong τ_{had} candidates satisfying the "tight" working point criteria are considered. This working point is roughly 40% efficient for one-prong τ_{had} candidates originating from W-boson or Z-boson decays, and has a jet rejection factor of roughly 300. Additional requirements to remove τ_{had} candidates initiated by prompt electrons or muons are also imposed.

Since lepton and jet candidates can be reconstructed as multiple objects, the following logic is applied to remove overlaps. If two electrons are separated by $\Delta R < 0.1$, the candidate with lower p_{T} is neglected. If a jet lies within $\Delta R = 0.2$ of an electron or τ_{had} candidate, the jet is neglected, while if the separation of the jet from an electron candidate satisfies $0.2 \leq \Delta R < 0.4$, the electron is neglected. In addition, electrons within $\Delta R = 0.1$ of a muon are also neglected, as are τ_{had} candidates within $\Delta R = 0.2$ of electron or muon candidates. Finally, muon candidates with a jet within $\Delta R = 0.4$ are neglected.

5 Signal Regions

Events satisfying all selection criteria are classified into four categories. Events in which at least three of the lepton candidates are electrons or muons are selected first, followed by events with two electrons or muons, or one of each, and at least one τ_{had} candidate. These two categories are referred to as $\geq 3e/\mu$ and $2e/\mu+ \geq 1\tau_{\mathrm{had}}$ respectively. Next, events in each of those two categories are sub-divided by the presence or absence of a reconstructed Z-boson candidate, which is defined as an opposite-sign same-flavor pair of lepton candidates with a total invariant mass within ±20 GeV of the Z-boson mass [56]. An additional electron may also be included in the combination with the same-flavor opposite-sign pair to satisfy the invariant mass requirement, to handle cases where an energetic photon from final-state radiation converts

Variable	Signal Region Definition				Additional Requirements
$H_{\mathrm{T}}^{\mathrm{leptons}}$	Inclusive	≥200 GeV	≥ 500 GeV	≥ 800 GeV	
Min. p_{T}^{ℓ}	Inclusive	≥ 50 GeV	≥ 100 GeV	≥ 150 GeV	
$E_{\mathrm{T}}^{\mathrm{miss}}$	Inclusive	≥100 GeV	≥ 200 GeV	≥ 300 GeV	$H_{\mathrm{T}}^{\mathrm{jets}} < 150$ GeV
$E_{\mathrm{T}}^{\mathrm{miss}}$	Inclusive	≥100 GeV	≥ 200 GeV	≥ 300 GeV	$H_{\mathrm{T}}^{\mathrm{jets}} \geq 150$ GeV
m_{eff}	Inclusive	≥600 GeV	≥1000 GeV	≥1500 GeV	
m_{eff}	Inclusive	≥600 GeV	≥1200 GeV		$E_{\mathrm{T}}^{\mathrm{miss}} \geq 100$ GeV
m_{eff}	Inclusive	≥600 GeV	≥1200 GeV		$m_{\mathrm{T}}^{W} \geq 100$ GeV, on-Z
b-tags	Inclusive	≥ 1	≥ 2		

Table 1: Kinematic signal regions defined in the analysis.

in the detector and is reconstructed as a prompt electron. Events with a reconstructed Z-boson candidate are referred to as on-Z, and those without such a candidate are referred to as off-Z. The resulting four categories are mutually exclusive.

Several kinematic variables are used to characterize the events that satisfy all selection criteria. The variable $H_{\mathrm{T}}^{\mathrm{leptons}}$ is defined as the scalar sum of transverse momenta, or $p_{\mathrm{T}}^{\mathrm{vis}}$ for τ_{had} candidates, of the three leading leptons. The variable Min. p_{T}^{ℓ} is defined as the minimum p_{T} of the three leading leptons in the event. The variable $H_{\mathrm{T}}^{\mathrm{jets}}$ is defined as the sum of transverse momenta of all selected jets in the event. The "effective mass", m_{eff}, is the scalar sum of $E_{\mathrm{T}}^{\mathrm{miss}}$, $H_{\mathrm{T}}^{\mathrm{jets}}$, and the transverse momenta of all identified leptons in the event. For events classified as on-Z, the transverse mass using the $E_{\mathrm{T}}^{\mathrm{miss}}$ and the hardest lepton not associated with a Z-boson candidate is defined as:

$$m_{\mathrm{T}}^{W} = \sqrt{2 p_{\mathrm{T}}^{\ell} E_{\mathrm{T}}^{\mathrm{miss}} (1 - \cos(\Delta\phi))} \tag{1}$$

where $\Delta\phi$ is the ϕ separation of ℓ and $E_{\mathrm{T}}^{\mathrm{miss}}$.

Subsets of selected events are defined based on kinematic properties. The $H_{\mathrm{T}}^{\mathrm{leptons}}$ distribution is considered for all events in each category. The $E_{\mathrm{T}}^{\mathrm{miss}}$ distribution is considered separately for events with $H_{\mathrm{T}}^{\mathrm{jets}}$ below and above 150 GeV, which serves to separate events produced through weak and strong interactions. The m_{eff} distribution is considered for events with and without a requirement of $E_{\mathrm{T}}^{\mathrm{miss}} \geq 100$ GeV and with and without a requirement of $m_{\mathrm{T}}^{W} \geq 100$ GeV. Signal regions are also defined based on the number of b-jets. Increasing lower bounds on the value of each kinematic variable define signal regions; the lower bounds are shown in Table 1.

6 Background estimation

Standard Model processes that produce events with three or more lepton candidates fall into three classes. The first consists of events in which prompt leptons are produced in the hard interaction, including the WZ, ZZ, and $t\bar{t} + W/Z$ processes. A second class of events includes Drell–Yan production in association with an energetic γ, which then converts in the detector to produce a single reconstructed electron. A third class of events arises from non-prompt, non-isolated, or fake lepton candidates satisfying the identification criteria described in Section 4.

The first class of backgrounds is dominated by $WZ \to \ell\nu\ell'\ell'$ and $ZZ \to \ell\ell\ell'\ell'$ events. Smaller contributions come from $t\bar{t} + W \to b\bar{b}\ell\nu\ell'\nu\ell''\nu$ and $t\bar{t} + Z \to b\bar{b}\ell\nu\ell'\nu\ell''\ell''$ events. Contributions from triboson events, such as $WWW \to \ell\nu\ell'\nu\ell''\nu$ production, are negligible. All such processes are modeled with the dedicated MC samples described in Section 3. Reconstructed leptons in the simulated samples

are required to be consistent with the decay of a vector boson or tau lepton from the hard interaction. The second class of backgrounds, from Drell–Yan production in association with a hard photon, is also modeled with MC simulation.

The class of events that includes non-prompt or fake leptons, referred to here as the reducible background, is estimated using *in-situ* techniques which rely minimally on simulation. Such backgrounds for muons arise from semi-leptonic b- or c-hadron decays, from in-flight decays of pions or kaons, and from energetic jets that reach the muon spectrometer. Electron candidates can also arise from misidentified hadrons or jets. Hadronically decaying taus have large backgrounds from narrow, low-track-multiplicity jets that mimic τ_{had} signatures.

Relaxed criteria are defined for each lepton flavor. These criteria, in combination with a requirement that candidates fail the nominal identification criteria, produce samples of lepton candidates that are rich in background with minimal contributions from prompt leptons. For electron candidates, the relaxed criteria are defined using "loose" identification [33] or by a looser $|d_0/\sigma(d_0)|$ requirement. For muon candidates, the relaxed criteria are defined by relaxing the $|d_0/\sigma(d_0)|$ requirements and by a loose isolation requirement. The relaxed τ_{had} identification loosens the requirement on the LLH score.

Large samples of events are used to measure the ratio of the number of leptons satisfying the nominal identification criteria to the number that fail the nominal criteria but satisfy the relaxed criteria. This ratio can then be applied as a scale factor – referred to here as a "fake factor" – to multilepton events satisfying the relaxed criteria to estimate the background in signal regions. For electrons, the sample used to measure the fake factor is collected using prescaled loose electron and photon triggers with thresholds varying from 5 GeV to 200 GeV. Events with two oppositely-charged electrons with invariant mass consistent with a Z-boson, or with $m_{ee} < 20$ GeV are rejected to reduce the contamination from Drell–Yan processes. Events with $E_{\text{T}}^{\text{miss}} > 40$ GeV or with $m_{\text{T}}^{W} > 40$ GeV are rejected to reduce the contamination from W+jets events. The fake factors are parametrized two-dimensionally as functions of the p_{T} and η of the candidates. For muons, the sample used to measure the fake factor is collected with a dimuon trigger with a threshold of 13 GeV on both the muons. The tau fake factors are measured in a $W \to \mu\nu$(+jets) sample, where the composition and kinematics of the jets are similar to those in Z+jet events, the primary source of background in the τ_{had} channels. The muon used to tag the events and τ_{had} candidates used as the probe. The muon and tau fake factors are parametrized one-dimensionally as functions of p_{T} or η. The electron and muon fake factors also show a dependence on the jet multiplicity of the event. Corrections are derived for this dependence separately for electrons and muons.

Contributions from prompt leptons can bias the reducible background estimates in two ways. The first arises when prompt leptons populate either the tight or relaxed regions when deriving the fake factors. The second arises when prompt leptons populate the relaxed region when applying the fake factors. In all cases, the effects of prompt leptons on the reducible background estimates are evaluated and corrected using MC simulation.

The background estimates are tested in several control regions. The τ_{had} background estimates are tested by constructing a $Z \to \tau\tau \to \mu\tau_{\text{had}}$ control region, defined by the following selection:

- $p_T^{\mu} < 40$ GeV
- $42 < m_Z^{\text{vis.}} < 82$ GeV
- $m_{\text{T}}^{W} < 50$ GeV
- $\Delta\phi(\mu, \tau_{\text{had}}) > 2.4$
- $\cos\Delta\phi(\mu, E_{\text{T}}^{\text{miss}}) + \cos\Delta\phi(\tau, E_{\text{T}}^{\text{miss}}) > -0.15$

This selection is used to suppress the fake τ_{had} contributions to test the prompt τ_{had} with sufficient precision [55].

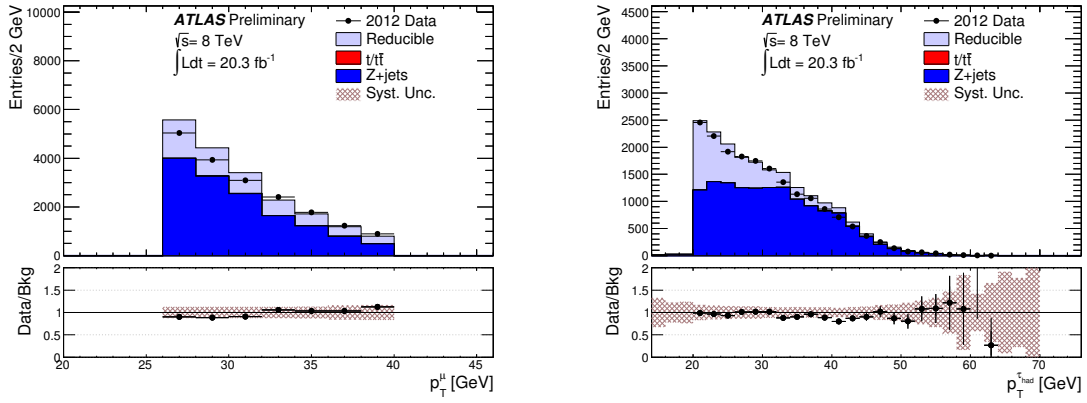

(a) (b)

Figure 1: The p_{T} distribution of the (a) muon and (b) τ_{had} in the $Z \to \mu\tau_{\mathrm{had}}$ control region. The bottom panel shows the ratio of events observed in data to those expected from background sources for each bin.

A control region rich in $t\bar{t}$ events is defined to test the reducible background estimates. Events in this region have exactly two identified lepton candidates with the same charge, at least one b-tag, and $H_{\mathrm{T}}^{\mathrm{jets}} \leq 500$ GeV. If the two leptons are electrons or muons (i.e. $e^{\pm}e^{\pm}$, $\mu^{\pm}\mu^{\pm}$, or $e^{\pm}\mu^{\pm}$), then the control region is referred to as the $t\bar{t}$-(e/μ) control region. If the lepton pair is $\mu\tau_{\mathrm{had}}$, the control region is the $t\bar{t}$-$(\mu\tau_{\mathrm{had}})$ control region. This sample is estimated to be primarily composed of lepton+jets $t\bar{t}$ events. The same-sign requirement suppresses events where both W bosons decay leptonically, and enhances the contributions from events where one lepton candidate originates from semileptonic b decay. The upper limit on $H_{\mathrm{T}}^{\mathrm{jets}}$ of 500 GeV reduces potential contamination from new phenomena.

Additional control regions to test the fake estimation techniques are defined by modifying the nominal selection of the leptons, remeasuring fake factors for the modified selection, and estimating the expected background.

Good agreement between the expected and observed event yields is seen in all control regions. Figure 1 shows the p_{T} distribution of the muon and the τ_{had} in the $Z \to \mu\tau_{\mathrm{had}}$ control region. Figure 2 shows the p_{T} distribution for the leading and subleading leptons in the $t\bar{t}$-(e/μ) control region. Figure 3 shows the m_{eff} distribution for the $t\bar{t}$ control region. The $H_{\mathrm{T}}^{\mathrm{leptons}}$ and $E_{\mathrm{T}}^{\mathrm{miss}}$ distributions are not shown here, but are also in good agreement in the control regions. Figure 4 shows the m_{T}^{W} distribution of the $E_{\mathrm{T}}^{\mathrm{miss}}$ and the lepton not associated with the Z boson candidate in the on-Z, $\geq 3e/\mu$ and $2e/\mu+ \geq 1\tau_{\mathrm{had}}$ channels, and provides validation for the modeling of the diboson background in the $\geq 3e/\mu$ channel.

7 Systematic uncertainties

The backgrounds modeled with simulated samples have uncertainties associated with trigger efficiencies, lepton efficiencies, lepton momentum scales and resolution, jet energy scales and resolution, and the luminosity uncertainty. The uncertainty on the $E_{\mathrm{T}}^{\mathrm{miss}}$ in simulation is computed from varying the inputs to the $E_{\mathrm{T}}^{\mathrm{miss}}$ calculation within their uncertainties on the energy/momentum scale and resolution, and is thus strongly correlated with the other uncertainties and not presented separately. Contributions to the $E_{\mathrm{T}}^{\mathrm{miss}}$ from soft activity not associated with high-p_{T} objects are presented separately. Uncertainties on the jet energy scale and resolution are significant in regions requiring large values of $H_{\mathrm{T}}^{\mathrm{jets}}$ or m_{eff}, and are small otherwise.

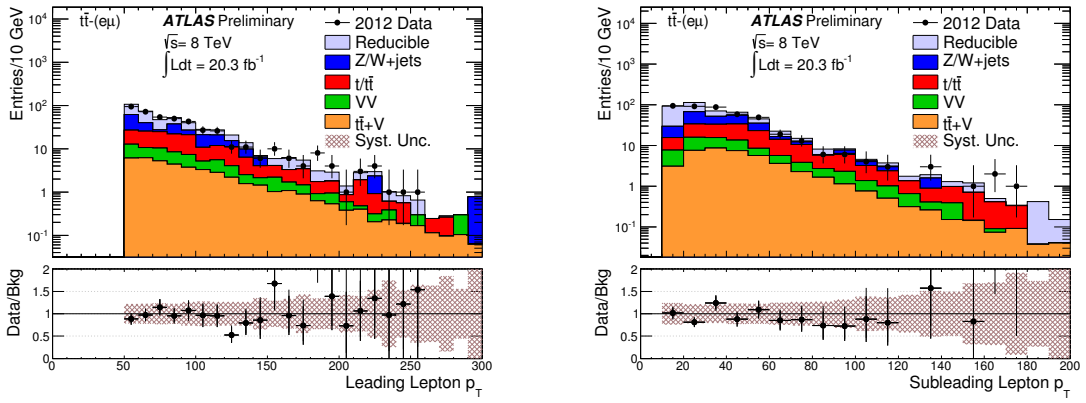

(a) (b)

Figure 2: The p_{T} distribution of the (a) leading and (b) subleading lepton in the $t\bar{t}$-($e\mu$) control region. The last bin shows the overflows. The bottom panel shows the ratio of events observed in data to those expected from background sources for each bin.

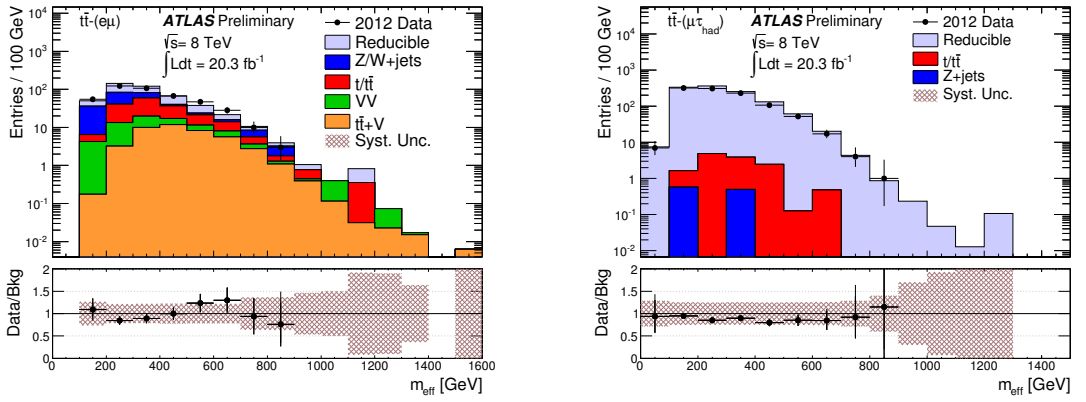

(a) (b)

Figure 3: The m_{eff} distribution for the (a) $t\bar{t}(e\mu)$ and (b) $t\bar{t}$-($\mu\tau_{\mathrm{had}}$) control regions. The last bin shows the overflows. The bottom panel shows the ratio of events observed in data to those expected from background sources for each bin.

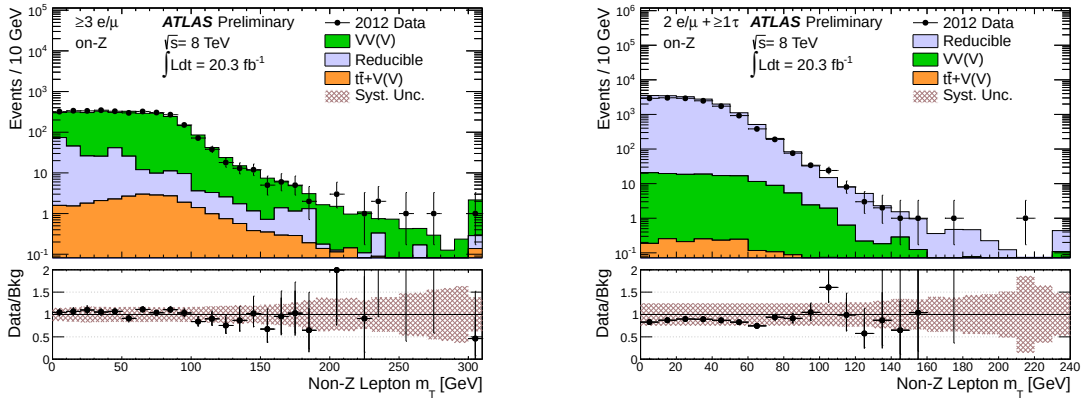

(a) (b)

Figure 4: The m_{T} distribution of the $E_{\mathrm{T}}^{\mathrm{miss}}$ and the lepton not associated with the Z-boson candidate decay in (a) $\geq 3e/\mu$ events and (b) $2e/\mu+ \geq 1\tau_{\mathrm{had}}$ events. The last bin shows the overflows. The bottom panel shows the ratio of events observed in data to those expected from background sources for each bin.

Uncertainties on the cross sections of the different Standard Model processes modeled by simulation are also considered. The SHERPA predictions of the WZ and ZZ processes are cross-checked with the next-to-leading-order predictions from POWHEG in a kinematic region similar to the signal regions considered in this search, resulting in 10% and 25% uncertainties in the normalization, respectively. Uncertainties from renormalization and factorization scale variations, as well as the variation of the parton distribution functions, contribute an additional 10% and 7% respectively, taken from Ref. [57]. An additional uncertainty of (150%)×($H_{\mathrm{T}}^{\mathrm{jets}}$ [TeV]) is applied to cover differences in jet activity between SHERPA and POWHEG. The $t\bar{t}+W$ and $t\bar{t}+Z$ backgrounds carry a total uncertainty of 30% based on parton distribution function and scale variations, and on large higher-order corrections [39, 40]. The Drell–Yan samples have a total uncertainty of 7% [58].

The reducible background estimates carry large uncertainties from several sources. The electron fake factors have uncertainties that range from 24% to 30% as a function of the candidate p_{T} while for muons the uncertainties range from 25% to 50%. The dominant source of uncertainty is the difference in sample composition in the region where the fake factors are measured and in the region where they are applied. The next dominant source of uncertainty for electrons is from the subtraction of prompt contamination; for muons, it is the dependence of the fake factors on the event jet multiplicity. For the τ_{had} fake estimates, a 25% uncertainty on the fake factors is determined which is dominated by the composition of the W+jets sample used for the fake rate measurement and the contamination of Z+jets in that sample. In signal regions where the relaxed samples are poorly populated, statistical uncertainties on the reducible background estimates become significant, especially in regions with high $E_{\mathrm{T}}^{\mathrm{miss}}$ or $H_{\mathrm{T}}^{\mathrm{jets}}$ requirements.

In all of the signal regions under study, the dominant systematic uncertainties on the total background estimate arise from the uncertainty associated with the reducible background estimates or from the uncertainty on the cross sections used for backgrounds taken from MC simulation.

Flavor Chan.	Z Chan.	Expected			Observed
$\geq 3e/\mu$	off-Z	260 $\pm$	10 $\pm$	40	280
$2e/\mu+ \geq 1\tau_{\text{had}}$	off-Z	1200 $\pm$	10 $\pm$	290	1193
$\geq 3e/\mu$	on-Z	3100 $\pm$	40 $\pm$	500	3199
$2e/\mu+ \geq 1\tau_{\text{had}}$	on-Z	17000 $\pm$	40 $\pm$	4000	14733

Table 2: The expected and observed event yields for all inclusive signal channels. The expected yields are presented with two uncertainties, the first is the statistical uncertainty, and the second is the systematic uncertainty.

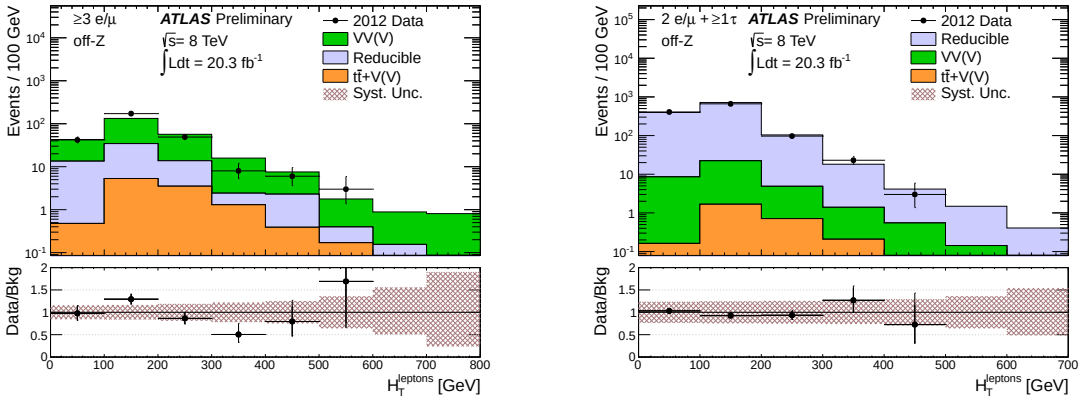

(a) (b)

Figure 5: The $H_{\text{T}}^{\text{leptons}}$ distribution for the off-Z (a) $\geq 3e/\mu$ and (b) $2e/\mu+ \geq 1\tau_{\text{had}}$ signal channels. The last bin shows the overflows. The bottom panel shows the ratio of events observed in data to those expected from background sources for each bin.

8 Results

Event yields for the most inclusive signal regions in each search channel are presented in Table 2. No significant deviation from the expected background is observed. The yields for all signal regions are presented in Tables 6–13 of Appendix A.

The $H_{\text{T}}^{\text{leptons}}$ distributions for the two off-Z signal channels are shown in Fig. 5, and the $E_{\text{T}}^{\text{miss}}$ distributions for the same channels are shown in Fig. 6. In that figure, the largest single bin excess is found in the $E_{\text{T}}^{\text{miss}}$ range of 180 – 200 GeV. This deviation corresponds to 2.4σ, taking into account statistical and systematic uncertainties. The m_{eff} distributions for the two on-Z channels are shown in Fig. 7.

The observed event yields in different signal regions are used to constrain contributions from new phenomena. The 95% confidence level (CL) upper limits on the number of events from non-Standard-Model sources (N_{95}) are calculated using the CL$_s$ method [59]. All statistical and systematic uncertainties on estimated backgrounds are incorporated into the limit-setting procedure, with correlations taken into account where appropriate. Systematic uncertainties of 10% (20%) on the signal efficiency are also included for the $\geq 3e/\mu$ ($2e/\mu+ \geq 1\tau_{\text{had}}$) channels, as described in Section 9. The N_{95} limits are then converted into limits on the "visible cross section" (σ_{95}^{vis}) using the relationship $\sigma_{95}^{\text{vis}} = N_{95}/\int Ldt$.

Figures 8–15 show the resulting observed limits, along with the median expected limits with $\pm 1\sigma$ and $\pm 2\sigma$ uncertainties. Figure 16 shows the deviations of all observed limits from the corresponding

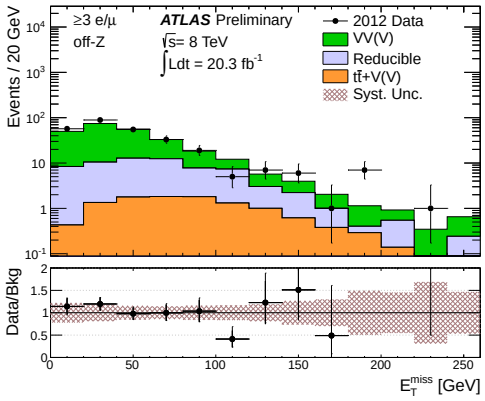

(a)

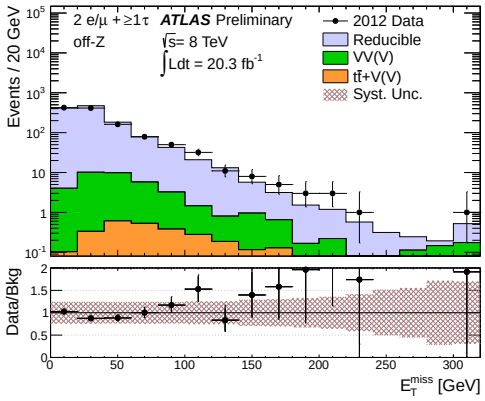

(b)

Figure 6: The $E_{\mathrm{T}}^{\mathrm{miss}}$ distribution for the off-Z (a) $\geq 3e/\mu$ and (b) $2e/\mu+ \geq 1\tau_{\mathrm{had}}$ signal channels. The last bin shows the overflows. The bottom panel shows the ratio of events observed in data to those expected from background sources for each bin.

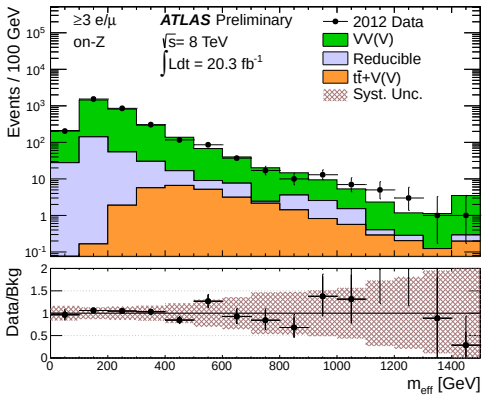

(a)

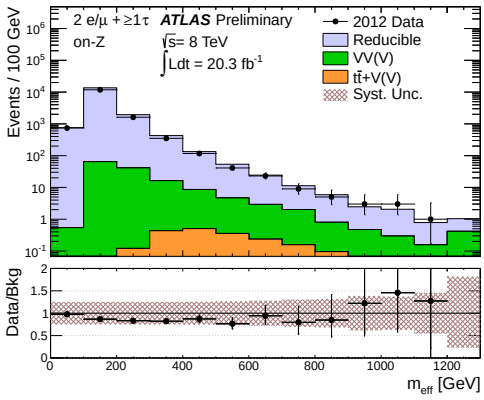

(b)

Figure 7: The m_{eff} distribution for the on-Z (a) $\geq 3e/\mu$ and (b) $2e/\mu+ \geq 1\tau_{\mathrm{had}}$ signal channels. The last bin shows the overflows. The bottom panel shows the ratio of events observed in data to those expected from background sources for each bin.

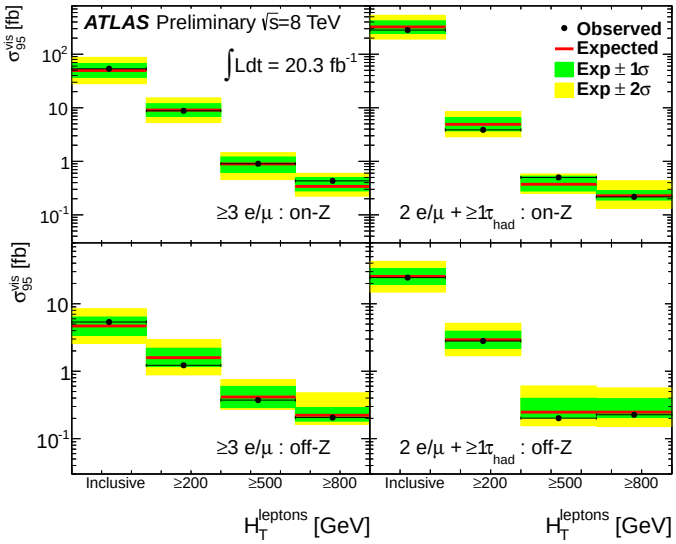

Figure 8: The observed- and median-expected 95% CL limit on the visible cross section (σ_{95}^{vis}) in the different signal channels, as functions of increasing lower bounds on $H_{\text{T}}^{\text{leptons}}$. The $\pm 1\sigma$ and $\pm 2\sigma$ uncertainties on the median expected limit are indicated by green and yellow bands, respectively.

expected limits – no significant deviation is observed in any signal region under study. Observed and expected limits are also presented in Tables 14–21 of Appendix B. The most inclusive signal regions for $H_{\text{T}}^{\text{leptons}}$, minimum p_{T}^{ℓ}, m_{eff}, and number of b-tags are composed of the same events within each channel, leading to identical limits.

9 Model testing

The σ_{95}^{vis} limits can be converted into upper limits on the cross section of a specific model as follows:

- Events from the new model are examined at the particle (MC-generator) level and kinematic requirements on the particles are applied. These include the p_{T} and η requirements for leptons and jets, and isolation requirements for the leptons. No special treatment for pileup is necessary.
- The number of events passing this selection determines the cross section for the model given the fiducial constraints, σ^{fid}.
- A correction factor must be applied to take into account detector effects. This correction factor, called ϵ_{fid}, is model-dependent, and is subject to uncertainties from detector resolution, reconstruction efficiency, pileup, and vertex selection. This correction factor represents the ratio of the number of events satisfying the selection criteria after reconstruction to all those satisfying the fiducial acceptance criteria at the particle level.
- A 95% CL upper-limit on the cross section in the new model is then given by:

$$\sigma_{95}^{\text{fid}} = \frac{N_{95}}{\epsilon_{fid} \int L\mathrm{d}t} = \frac{\sigma_{95}^{\text{vis}}}{\epsilon_{fid}}. \tag{2}$$

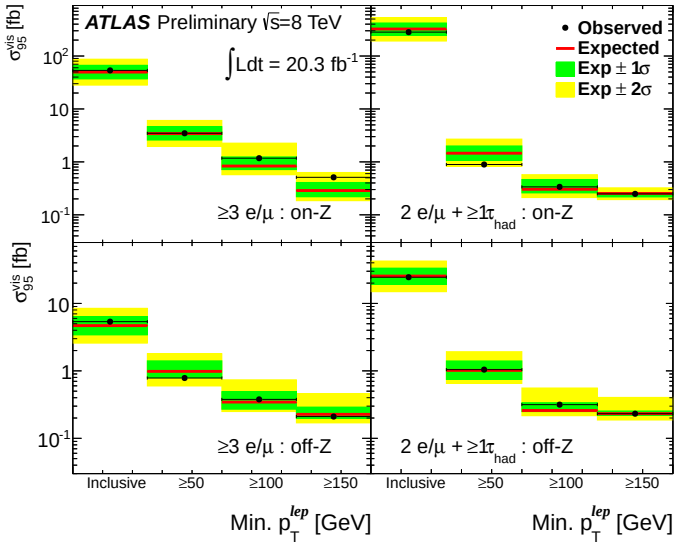

Figure 9: The observed- and median-expected 95% CL limit on the visible cross section ($\sigma_{95}^{\mathrm{vis}}$) in the different signal channels, as functions of increasing lower bounds on minimum p_{T}^{ℓ}. The $\pm 1\sigma$ and $\pm 2\sigma$ uncertainties on the median expected limit are indicated by green and yellow bands, respectively.

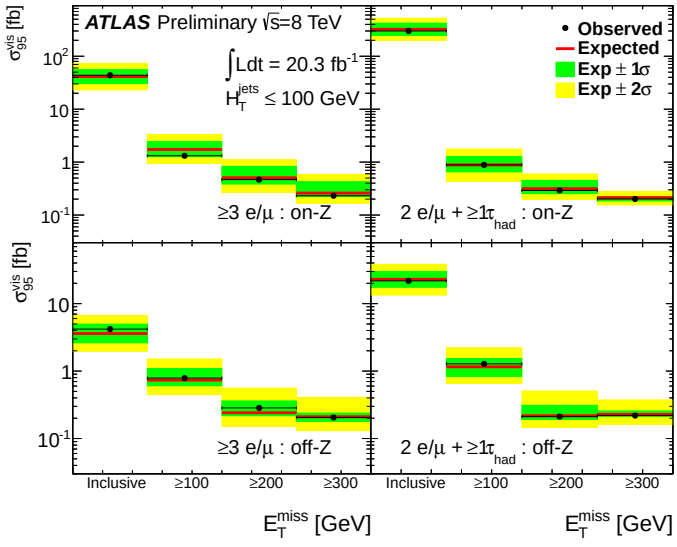

Figure 10: The observed- and median-expected 95% CL limit on the visible cross section ($\sigma_{95}^{\mathrm{vis}}$) in the different signal channels, as functions of increasing lower bounds on $E_{\mathrm{T}}^{\mathrm{miss}}$, for events with $H_{\mathrm{T}}^{\mathrm{jets}} < 150$ GeV. The $\pm 1\sigma$ and $\pm 2\sigma$ uncertainties on the median expected limit are indicated by green and yellow bands, respectively.

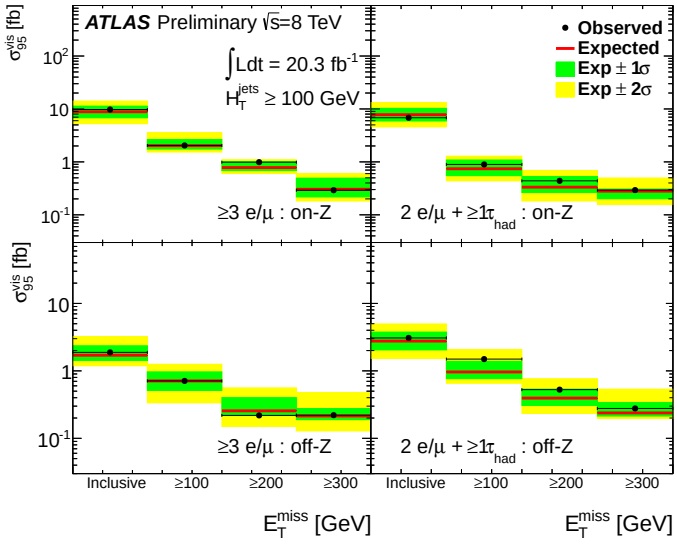

Figure 11: The observed- and median-expected 95% CL limit on the visible cross section ($\sigma_{95}^{\mathrm{vis}}$) in the different signal channels, as functions of increasing lower bounds on $E_{\mathrm{T}}^{\mathrm{miss}}$, for events with $H_{\mathrm{T}}^{\mathrm{jets}} \geq 150$ GeV. The $\pm 1\sigma$ and $\pm 2\sigma$ uncertainties on the median expected limit are indicated by green and yellow bands, respectively.

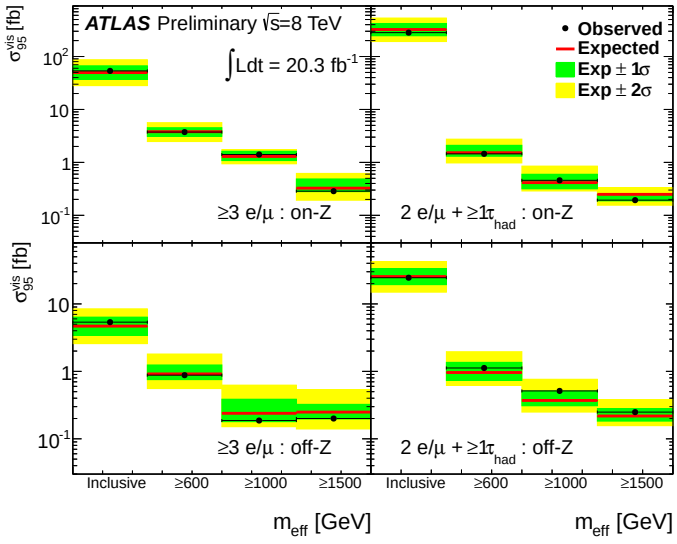

Figure 12: The observed- and median-expected 95% CL limit on the visible cross section ($\sigma_{95}^{\mathrm{vis}}$) in the different signal channels, as functions of increasing lower bounds on m_{eff}. The $\pm 1\sigma$ and $\pm 2\sigma$ uncertainties on the median expected limit are indicated by green and yellow bands, respectively.

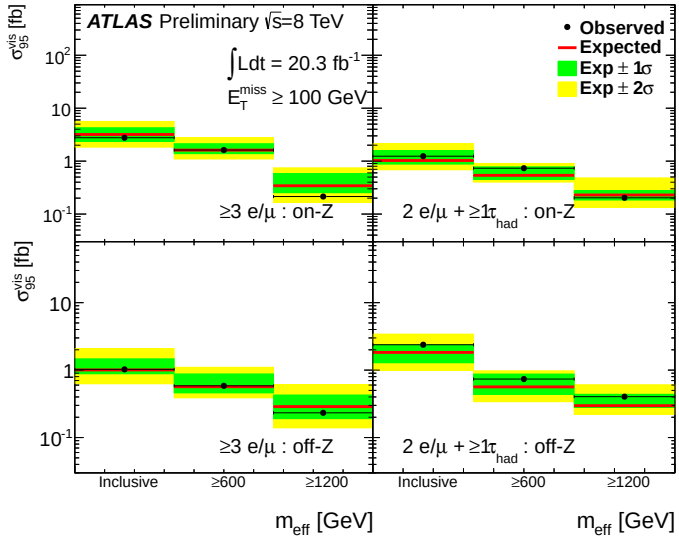

Figure 13: The observed- and median-expected 95% CL limit on the visible cross section ($\sigma_{95}^{\mathrm{vis}}$) in the different signal channels, as functions of increasing lower bounds on m_{eff}, for events with $E_{\mathrm{T}}^{\mathrm{miss}} > 100$ GeV. The $\pm 1\sigma$ and $\pm 2\sigma$ uncertainties on the median expected limit are indicated by green and yellow bands, respectively.

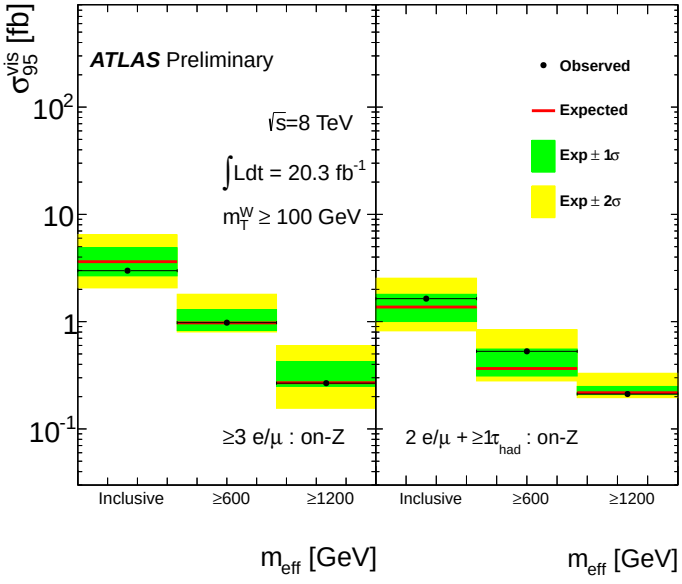

Figure 14: The observed- and median-expected 95% CL limit on the visible cross section ($\sigma_{95}^{\mathrm{vis}}$) in the different signal channels, as functions of increasing lower bounds on m_{eff}, for events with $m_{\mathrm{T}}^{W} > 100$ GeV. The $\pm 1\sigma$ and $\pm 2\sigma$ uncertainties on the median expected limit are indicated by green and yellow bands, respectively.

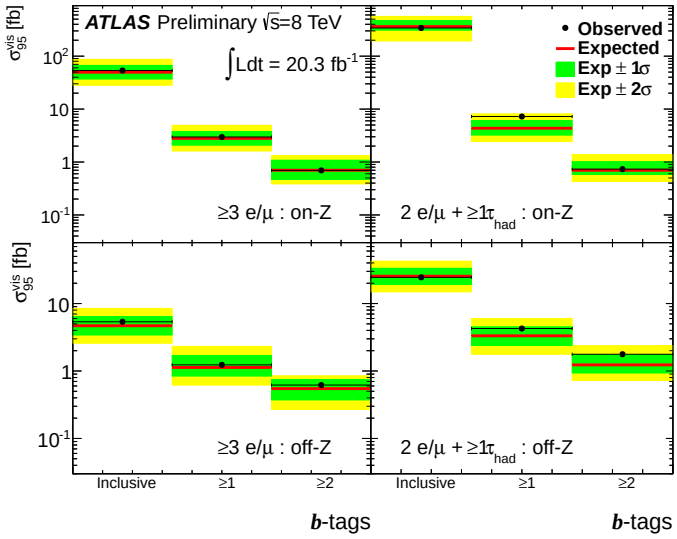

Figure 15: The observed- and median-expected 95% CL limit on the visible cross section ($\sigma_{95}^{\mathrm{vis}}$) in the different signal channels, as functions of increasing lower bounds on the number of b-tags. The $\pm 1\sigma$ and $\pm 2\sigma$ uncertainties on the median expected limit are indicated by green and yellow bands, respectively.

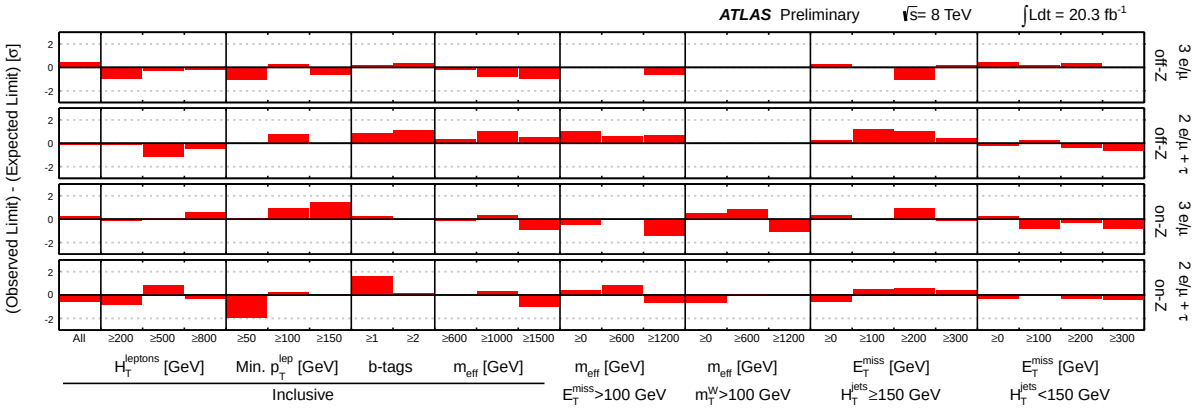

Figure 16: Deviations of observed limits from expected limits, in units of the total uncertainty on the expected limit, for all signal regions under study.

In order to determine ϵ_{fid} for unexplored models of new phenomena producing at least three prompt, isolated, and charged leptons in the final state, per-lepton efficiencies parametrized by the lepton kinematics are provided here. While the experimental results are based on reconstructed quantities, all requirements in the following are defined at the particle level.

Electrons at the particle level are required to have $p_{\mathrm{T}} \geq 10$ GeV, and to satisfy $|\eta| < 2.47$ and $|\eta| \notin (1.37, 1.52)$. Particle-level muons are required to have $p_{\mathrm{T}} \geq 10$ GeV, and to have $|\eta| < 2.5$. Electrons and muons are both required to be prompt, and not associated with a secondary vertex, unless they are the product of tau-lepton decays. Leptonically decaying tau candidates are required to produce electrons or muons that satisfy the criteria above. Hadronically decaying tau candidates are required to have $p_{\mathrm{T}}^{\mathrm{vis}} \geq 15$ GeV and $|\eta^{\mathrm{vis}}| < 2.5$, where the visible products of the tau decay include all particles except neutrinos. As with reconstructed tau candidates, the tau four-momentum at the particle level is defined only by the visible decay products.

Generated electrons and muons are further required to be isolated. A track isolation energy at the particle level corresponding to $p_{\mathrm{T,track}}^{\mathrm{iso}}$, denoted $p_{\mathrm{T,true}}^{\mathrm{iso}}$, is defined as the scalar sum of transverse momenta of charged particles within a cone of $\Delta R < 0.3$ around the lepton axis. Particles used in the sum are included after hadronization and must have $p_{\mathrm{T}} > 1$ GeV. A fiducial isolation energy corresponding to $E_{\mathrm{T,cal}}^{\mathrm{iso}}$, denoted $E_{\mathrm{T,true}}^{\mathrm{iso}}$, is defined as the sum of all particles inside the annulus $0.1 < \Delta R < 0.3$ around the lepton axis. Neutrinos and other stable, weakly-interacting particles are excluded from both $p_{\mathrm{T,true}}^{\mathrm{iso}}$ and $E_{\mathrm{T,true}}^{\mathrm{iso}}$; muons are excluded from $E_{\mathrm{T,true}}^{\mathrm{iso}}$. Electrons and muons must satisfy $p_{\mathrm{T,true}}^{\mathrm{iso}}/p_{\mathrm{T}} < 0.15$ and $E_{\mathrm{T,true}}^{\mathrm{iso}}/p_{\mathrm{T}} < 0.15$.

Events with at least three leptons as defined above must have at least two electrons and/or muons, at least one of which has $p_{\mathrm{T}} \geq 25$ GeV. The third lepton is allowed to be an electron or muon, in which case the event is classified as a $\geq 3e/\mu$ event, or a hadronically decaying tau lepton, in which case it is a $2e/\mu+ \geq 1\tau_{\mathrm{had}}$ event.

A simulated sample of WZ events is used to determine the per-lepton efficiencies ϵ_ℓ. The leptons above are matched to reconstructed lepton candidates that satisfy the selection criteria defined in Section 4, with ϵ_ℓ defined as the ratio of the number of reconstructed leptons satisfying all selection criteria to the number of generated leptons satisfying the fiducial criteria. Separate values of ϵ_ℓ are measured for each lepton flavor. In the case of electrons and muons, ϵ_ℓ is determined separately for leptons from tau decays.

All efficiencies are measured as functions of the lepton p_{T} and η. The efficiencies for electrons and taus are shown in Tables 3 and 4. The η dependence of the muon efficiencies is treated by separate p_{T} efficiency measurements for muons with $|\eta| < 0.1$ and those with $|\eta| \geq 0.1$, and is shown in Table 5. For τ_h, the efficiency tables include the efficiency for τ_h generated with $p_{\mathrm{T}}^{\mathrm{vis}} < 20$ GeV but reconstructed with $p_{\mathrm{T}}^{\mathrm{vis}} \geq 20$ GeV, due to resolution effects. The corresponding efficiencies for electrons and muons generated below 15 GeV are much smaller. For empty bins, the value from the preceding bin is the suggested central value. The final per-lepton efficiency for electrons and taus is obtained as $\epsilon_\ell = \epsilon(p_{\mathrm{T}}) \cdot \epsilon(\eta)/\langle\epsilon\rangle$, where $\langle\epsilon\rangle$ is 0.66 for prompt electrons, 0.39 for electrons from tau decays, and 0.26 for hadronically decaying taus.

The resulting per-lepton efficiencies are then combined to yield a selection efficiency for a given event satisfying the fiducial acceptance criteria. For events with exactly three leptons, the total efficiency for the event is the product of the individual lepton efficiencies. For events with more than three leptons, the additional leptons in order of descending p_{T} only contribute to the total efficiency when a lepton with higher p_{T} is not selected, leading to terms like $\epsilon_1\epsilon_2\epsilon_4(1-\epsilon_3)$, where ϵ_i denotes the fiducial efficiency for the i^{th} p_{T}-ordered lepton. The method can be extended to cover the number of leptons expected by the model under consideration.

Jets at the particle level are reconstructed from all stable particles, excluding muons and neutrinos, with the anti-k_t algorithm using a distance parameter $R = 0.4$. Overlaps between jets and leptons are

p_{T} [GeV]	Prompt e	$\tau \to e$	τ_h
10–15	0.045±0.001	0.027±0.002	-
15–20	0.484±0.003	0.384±0.005	0.071±0.003
20–25	0.571±0.003	0.470±0.006	0.251±0.006
25–30	0.628±0.002	0.518±0.007	0.321±0.007
30–40	0.681±0.002	0.573±0.006	0.313±0.006
40–50	0.713±0.002	0.597±0.009	0.326±0.007
50–60	0.746±0.002	0.64±0.01	0.309±0.009
60–80	0.767±0.002	0.67±0.01	0.295±0.009
80–100	0.799±0.003	0.67±0.02	0.32±0.02
100–200	0.820±0.003	0.63±0.03	0.33±0.02
200–400	0.835±0.009	0.72±0.08	0.29±0.05
400–600	0.819±0.043	-	-
≥ 600	0.829±0.104	-	-

Table 3: The fiducial efficiency for electrons and taus in different p_{T} ranges. The uncertainties shown here are statistical only.

$\lvert\eta\rvert$	Prompt e	$\tau \to e$	τ_h
0.0–0.1	0.640±0.003	0.37±0.01	0.24±0.01
0.1–0.5	0.699±0.001	0.412±0.005	0.305±0.005
0.5–1.0	0.702±0.001	0.412±0.005	0.275±0.005
1.0–1.5	0.660±0.002	0.375±0.006	0.208±0.005
1.5–2.0	0.605±0.002	0.351±0.006	0.253±0.006
2.0–2.5	0.602±0.002	0.379±0.006	0.246±0.006

Table 4: The fiducial efficiency for electrons and taus in different η ranges. The uncertainties shown here are statistical only.

p_{T}	Prompt μ		$\tau \to \mu$	
[GeV]	$\lvert\eta\rvert > 0.1$	$\lvert\eta\rvert < 0.1$	$\lvert\eta\rvert > 0.1$	$\lvert\eta\rvert < 0.1$
10–15	0.021±0.001	0.003±0.002	0.013±0.001	0.005±0.003
15–20	0.704±0.003	0.37±0.01	0.539±0.005	0.29±0.02
20–25	0.808±0.002	0.42±0.01	0.620±0.006	0.35±0.03
25–30	0.855±0.002	0.45±0.01	0.675±0.007	0.39±0.03
30–40	0.896±0.001	0.498±0.008	0.708±0.006	0.42±0.03
40–50	0.920±0.001	0.515±0.008	0.754±0.008	0.42±0.04
50–60	0.932±0.001	0.515±0.009	0.78±0.01	0.49±0.05
60–80	0.940±0.001	0.528±0.009	0.78±0.01	0.46±0.05
80–100	0.938±0.002	0.51±0.01	0.74±0.02	0.42±0.08
100–200	0.939±0.002	0.53±0.01	0.81±0.02	0.4±0.1
200–400	0.936±0.006	0.52±0.05	0.91±0.06	-
400–600	0.95±0.02	0.5±0.2	-	-
≥ 600	0.92±0.08	-	-	-

Table 5: The fiducial efficiency for muons in different p_{T} ranges. The uncertainties shown here are statistical only.

removed as described in Section 4. $E_{\mathrm{T}}^{\mathrm{miss}}$ is defined as the magnitude of the vector sum of the transverse momenta of all stable, weakly-interacting particles, including those produced in models of new phenomena. The kinematic variables used for limit setting are defined as before: $H_{\mathrm{T}}^{\mathrm{leptons}}$ is the scalar sum of the transverse momenta, or $p_{\mathrm{T}}^{\mathrm{vis}}$ for τ_{had} candidates, of the three leptons that define the event; $H_{\mathrm{T}}^{\mathrm{jets}}$ is the scalar sum of all jets surviving overlap removal; $E_{\mathrm{T}}^{\mathrm{miss}}$ is as defined above, and m_{eff} is the sum of $E_{\mathrm{T}}^{\mathrm{miss}}$, $H_{\mathrm{T}}^{\mathrm{jets}}$, and all transverse momenta of selected leptons in the event.

Predictions of the rate and kinematic properties of events with multiple leptons made with the method described above agree well with the same quantities after detector simulation for the chosen models of new phenomena: doubly-charged Higgs of various masses and vector-like B quarks [60]. Uncertainties, based on the level of agreement seen across the studied models, are estimated at 10% for the $\geq 3e/\mu$ channels, and 20% for the $2e/\mu+ \geq 1\tau_{\mathrm{had}}$ channels. These uncertainties are included in the limits presented in Section 8.

10 Conclusion

A generic search for new phenomena in events with at least three energetic, charged, prompt, and isolated leptons has been presented, using a data sample corresponding to an integrated luminosity of 20.3 fb^{-1} of pp collision data at a center-of-mass energy of $\sqrt{s} = 8$ TeV collected by the ATLAS experiment. The search was conducted in separate channels based on the presence or absence of a hadronically decaying tau lepton or the presence of a reconstructed Z boson, and yielded no significant deviation from background yields expected from the Standard Model. Upper limits at 95% confidence level on event yields due to non-Standard-Model processes were placed as a function of lower bounds on several kinematic variables. Additional information on the fiducial selection of events populating the signal regions under study has been provided.

References

[1] S. Matsumoto, T. Nabeshima, and K. Yoshioka, *Seesaw Neutrino Signals at the Large Hadron Collider*, J. High Energy Phys. **1006** (2010) 058, arXiv:1004.3852 [hep-ph].

[2] A. Belyaev, C. Leroy, and R. R. Mehdiyev, *Production of excited neutrino at LHC*, Eur. Phys. J. **C41S2** (2005) 1–10, arXiv:0401066 [hep-ph].

[3] P. H. Frampton, P. Hung, and M. Sher, *Quarks and leptons beyond the third generation*, Phys. Rept. **330** (2000) 263, arXiv:9903387 [hep-ph].

[4] A. Zee, *Charged scalar field and quantum number violations*, Phys. Lett. **B161** (1985) 141 – 145.

[5] A. Zee, *Quantum numbers of Majorana neutrino masses*, Nucl. Phys. **B264** (1986) 99.

[6] K. S. Babu, *Model of calculable Majorana neutrino masses*, Phys. Lett. **B203** (1988) 132.

[7] H. Miyazawa, *Baryon Number Changing Currents*, Prog. Theor. Phys. **36 (6)** (1966) 1266–1276.

[8] P. Ramond, *Dual Theory for Free Fermions*, Phys. Rev. **D3** (1971) 2415–2418.

[9] Y. A. Gol'fand and E. P. Likhtman, *Extension of the Algebra of Poincare Group Generators and Violation of p Invariance*, JETP Lett. **13** (1971) 323–326. [Pisma Zh. Eksp. Teor. Fiz. 13:452-455,1971].

[10] A. Neveu and J. H. Schwarz, *Factorizable dual model of pions*, Nucl. Phys. **B31** (1971) 86–112.

[11] A. Neveu and J. H. Schwarz, *Quark Model of Dual Pions*, Phys. Rev. **D4** (1971) 1109–1111.

[12] J. Gervais and B. Sakita, *Field theory interpretation of supergauges in dual models*, Nucl. Phys. **B34** (1971) 632–639.

[13] D. V. Volkov and V. P. Akulov, *Is the Neutrino a Goldstone Particle?*, Phys. Lett. **B46** (1973) 109–110.

[14] J. Wess and B. Zumino, *A Lagrangian Model Invariant Under Supergauge Transformations*, Phys. Lett. **B49** (1974) 52.

[15] J. Wess and B. Zumino, *Supergauge Transformations in Four-Dimensions*, Nucl. Phys. **B70** (1974) 39–50.

[16] T. G. Rizzo, *Doubly Charged Higgs Bosons and Lepton Number Violating Processes*, Phys. Rev. **D25** (1982) 1355–1364.

[17] H. Georgi and M. Machacek, *Doubly Charged Higgs Bosons*, Nucl. Phys. **B262** (1985) 463.

[18] J. C. Montalvo, N. V. C. Jr., J. S. Borges, and M. D. Tonasse, *Searching for doubly charged Higgs bosons at the LHC in a 3-3-1 model*, Nucl. Phys. **B756** (2006) 1 – 15. Erratum: ibid. **796** 422 (2008).

[19] J. Gunion, R. Vega, and J. Wudka, *Higgs triplets in the standard model*, Phys.Rev. **D42** (1990) 1673–1691.

[20] R. Dalitz, *On an alternative decay process for the neutral pi-meson, Letters to the Editor*, Proc. Phys. Soc. **A64** (1951) 667–669.

[21] N. M. Kroll and W. Wada, *Internal pair production associated with the emission of high-energy gamma rays*, Phys. Rev. **98** (1955) 1355–1359.

[22] ATLAS Collaboration, *Search for new phenomena in events with three charged leptons at a center-of-mass energy of 7 TeV with the ATLAS detector*, Phys. Rev. **D87** (2013) 052002, arXiv:1211.6312 [hep-ex].

[23] CMS Collaboration, *Search for anomalous production of multilepton events in pp collisions at* $\sqrt{s} = 7$ *TeV*, J. High Energy Phys. **1206** (2012) 169, arXiv:1204.5341 [hep-ex].

[24] ATLAS Collaboration, *Search for direct production of charginos and neutralinos in events with three leptons and missing transverse momentum in* $\sqrt{s} = 7$ *TeV pp collisions with the ATLAS detector*, Phys.Lett. **B718** (2013) 841–859, arXiv:1208.3144 [hep-ex].

[25] ATLAS Collaboration, *Search for direct production of charginos and neutralinos in events with three leptons and missing transverse momentum in 21* fb^{-1} *of pp collisions at* $\sqrt{s} = 8$ *TeV with the ATLAS detector*, . http://cds.cern.ch/record/1532426.

[26] ATLAS Collaboration, *Search for supersymmetry using events with three leptons, multiple jets, and missing transverse momentum in 13.0* fb^{-1} *of pp collisions with the ATLAS detector at* $\sqrt{s} = 8$ *TeV*, . http://cds.cern.ch/record/1493490.

[27] CDF Collaboration, *Search for Supersymmetry in* $p\bar{p}$ *Collisions at* $\sqrt{s} = 1.96$*-TeV Using the Trilepton Signature of Chargino-Neutralino Production*, Phys. Rev. Lett. **101** (2008) 251801, arXiv:0808.2446 [hep-ex].

[28] D0 Collaboration, *Search for associated production of charginos and neutralinos in the trilepton final state using 2.3* fb^{-1} *of data*, Phys. Lett. **B680** (2009) 34–43, arXiv:0901.0646 [hep-ex].

[29] ATLAS Collaboration, *The ATLAS Experiment at the CERN Large Hadron Collider*, J. Instrumentation **3** (2008) S08003.

[30] ATLAS Collaboration, *Performance of the ATLAS Trigger System in 2010*, Eur. Phys. J. **C72** (2012) 1849, arXiv:1110.1530 [hep-ex].

[31] S. Agostinelli et al., *Geant4 – a simulation toolkit*, Nucl. Instrum. Methods **506** (2003) 250 – 303.

[32] ATLAS Collaboration, *The ATLAS Simulation Infrastructure*, Eur. Phys. J. **C70** (2010) 823–874, arXiv:1005.4568 [physics.ins-det].

[33] ATLAS Collaboration, *Electron performance measurements with the ATLAS detector using the 2010 LHC proton-proton collision data*, Eur. Phys. J. **C72** (2012) 1909, arXiv:1110.3174 [hep-ex].

[34] ATLAS Collaboration, *Muon reconstruction efficiency in reprocessed 2010 LHC proton-proton collision data recorded with the ATLAS detector*, ATLAS-CONF-2011-063 (2011) . http://cdsweb.cern.ch/record/1345743.

[35] T. Gleisberg, S. Hoeche, F. Krauss, M. Schonherr, S. Schumann, et al., *Event generation with SHERPA 1.1*, J. High Energy Phys. **0902** (2009) 007, arXiv:0811.4622 [hep-ph].

[36] T. Melia, P. Nason, R. Rontsch, and G. Zanderighi, *W+W-, WZ and ZZ production in the POWHEG BOX*, J. High Energy Phys. **1111** (2011) 078, arXiv:1107.5051 [hep-ph].

[37] J. Alwall, M. Herquet, F. Maltoni, O. Mattelaer, and T. Stelzer, *MadGraph 5 : Going Beyond*, J. High Energy Phys. **1106** (2011) 128, arXiv:1106.0522 [hep-ph].

[38] T. Sjöstrand, P. Edn, C. Friberg, L. Lnnblad, G. Miu, S. Mrenna, and N. Emanuel, *High-Energy-Physics Event Generation with* PYTHIA *6.1*, Comput. Phys. Comm. **135** (2001) 238, arXiv:0010017 [hep-ph].

[39] J. M. Campbell and R. K. Ellis, $t\bar{t}W^{+-}$ *production and decay at NLO*, J. High Energy Phys. **1207** (2012) 052, arXiv:1204.5678 [hep-ph].

[40] M. Garzelli, A. Kardos, C. Papadopoulos, and Z. Trocsanyi, Z^0 *- boson production in association with a top anti-top pair at NLO accuracy with parton shower effects*, Phys. Rev. **D85** (2012) 074022, arXiv:1111.1444 [hep-ph].

[41] M. L. Mangano, M. Moretti, F. Piccinini, R. Pittau, and A. D. Polosa, *ALPGEN, a generator for hard multiparton processes in hadronic collisions*, J. High Energy Phys. **0307** (2003) 001, arXiv:0206293 [hep-ph].

[42] G. Corcella, I. Knowles, G. Marchesini, S. Moretti, K. Odagiri, et al., *HERWIG 6: An Event generator for hadron emission reactions with interfering gluons (including supersymmetric processes)*, J. High Energy Phys. **0101** (2001) 010, arXiv:0011363 [hep-ph].

[43] J. Butterworth, J. R. Forshaw, and M. Seymour, *Multiparton interactions in photoproduction at HERA*, Z. Phys. **C72** (1996) 637–646, arXiv:9601371 [hep-ph].

[44] H.-L. Lai, M. Guzzi, J. Huston, Z. Li, P. M. Nadolsky, et al., *New parton distributions for collider physics*, Phys. Rev. **D82** (2010) 074024, arXiv:1007.2241 [hep-ph].

[45] A. Sherstnev and R. S. Thorne, *Parton Distributions for LO Generators*, Eur. Phys. J. **C55** (2008) 553–575, arXiv:0711.2473 [hep-ph].

[46] J. Pumplin, D. Stump, J. Huston, H. Lai, P. M. Nadolsky, et al., *New generation of parton distributions with uncertainties from global QCD analysis*, J. High Energy Phys. **0207** (2002) 012, arXiv:0201195 [hep-ph].

[47] P. M. Nadolsky, H.-L. Lai, Q.-H. Cao, J. Huston, J. Pumplin, et al., *Implications of CTEQ global analysis for collider observables*, Phys. Rev. **D78** (2008) 013004, arXiv:0802.0007 [hep-ph].

[48] ATLAS Collaboration, *Luminosity Determination in pp Collisions at* $\sqrt{s} = 7$ *TeV Using the ATLAS Detector at the LHC*, Eur. Phys. J. **C71** (2011) 1630, arXiv:1101.2185 [hep-ex].

[49] M. Cacciari, G. P. Salam, and G. Soyez, *FastJet User Manual*, Eur. Phys. J. **C72** (2012) 1896, arXiv:1111.6097 [hep-ph].

[50] M. Cacciari, G. P. Salam, and G. Soyez, *The anti-kt jet clustering algorithm*, J. High Energy Phys. **04** (2008) 063, arXiv:0802.1189 [hep-ph].

[51] ATLAS Collaboration, *Jet energy measurement with the ATLAS detector in proton-proton collisions at* $\sqrt{s} = 7$ *TeV*, Eur. Phys. J. **C73** (2013) 2304, arXiv:1112.6426 [hep-ex].

[52] ATLAS Collaboration, *Jet energy resolution and selection efficiency relative to track jets from in-situ techniques with the ATLAS Detector Using Proton-Proton Collisions at a Center of Mass Energy* $\sqrt{s} = 7$ *TeV*, ATLAS-CONF-2010-054 (2010) . http://cdsweb.cern.ch/record/1281311.

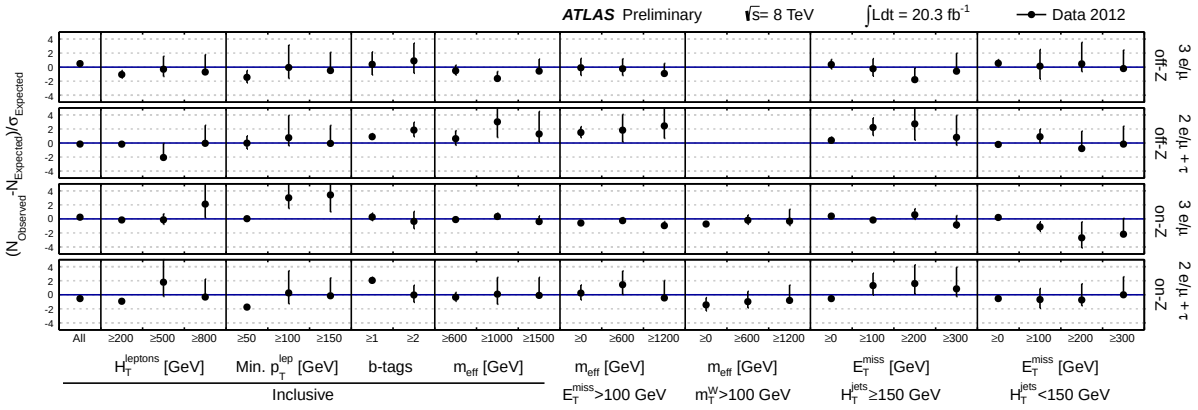

Figure 17: Deviations of observed yields from expected yields, in units of the total uncertainty on the expected yield, for all signal regions under study. For the most inclusive signal regions, see Table 2.

[53] ATLAS Collaboration, *Commissioning of the ATLAS high-performance b-tagging algorithms in the 7 TeV collision data*, ATLAS-CONF-2011-102 (2011) . http://cds.cern.ch/record/1369219.

[54] ATLAS Collaboration, *Measurement of the b-tag Efficiency in a Sample of Jets Containing Muons with 5 fb^{-1} of Data from the ATLAS Detector*, ATLAS-CONF-2012-043 (2012) . http://cds.cern.ch/record/1435197.

[55] ATLAS Collaboration, *Identification of Hadronic Decays of Tau Leptons in 2012 Data with the ATLAS Detector*, ATLAS-CONF-2013-064 (2013) .

[56] Particle Data Group Collaboration, J. Beringer et al., *Review of Particle Physics (RPP)*, Phys. Rev. **D86** (2012) 010001.

[57] ATLAS Collaboration, *Search for anomalous production of prompt like-sign muon pairs and constraints on physics beyond the Standard Model with the ATLAS detector*, Phys. Rev. **D85** (2012) 032004, arXiv:1201.1091 [hep-ex].

[58] ATLAS Collaboration, *Search for dilepton resonances in pp collisions at $\sqrt{s} = 7$ TeV with the ATLAS detector*, Phys. Rev. Lett. **107** (2011) 272002, arXiv:1108.1582 [hep-ex].

[59] A. L. Read, *Presentation of search results: the CL s technique*, J. of Phys. **G28** (2002) no. 10, 2693.

[60] ATLAS Collaboration, *Search for pair production of new heavy quarks that decay to a Z boson and a third generation quark in pp collisions at $\sqrt{s} = 8$ TeV with the ATLAS detector*, ATLAS-CONF-2013-056 (2013) . http://cdsweb.cern.ch/record/1557773.

A Tables of expected and observed event yields

$H_{\mathrm{T}}^{\mathrm{leptons}} \geq$ [GeV]	$t\bar{t}+V(V)$	$VV(V)$	Reducible	Total	Observed
$\geq 3e/\mu$, off-Z					
200	5.5 ±0.2 ±1.7	64 ±1 ±15	13.6 ±1.9 ±2.3	83 ±2 ±16	66
500	0.29 ±0.04 ±0.09	2.9 ±0.2 ±1.4	0.29 ±0.23 ±0.69	3.5 ±0.3 ±1.5	3
800	0.02 ±0.01 ±0.01	0.5 ±0.1 ±0.2	$0\ ^{+0.69}_{-0}$	0.5 ±0.1 ±0.7	0
$2e/\mu+ \geq 1\tau$, off-Z					
200	1.01 ±0.07 ±0.31	6.0 ±0.2 ±1.3	121 ±3 ±31	128 ±3 ±31	123
500	0.02 ±0.01 ±0.01	0.14 ±0.02 ±0.03	1.7 ±0.4 ±0.8	1.9 ±0.4 ±0.8	0
800	0.00 ±0.00 ±0.00	0.01 ±0.00 ±0.00	0.02 ±0.03 ±0.71	0.03 ±0.03 ±0.71	0
$\geq 3e/\mu$, on-Z					
200	12.1 ±0.2 ±3.6	389 ±4 ±98	28 ±4 ±6	429 ±6 ±99	414
500	0.46 ±0.05 ±0.14	11.0 ±0.6 ±5.3	2.2 ±1.3 ±0.7	13.7 ±1.5 ±5.3	13
800	0.03 ±0.01 ±0.01	0.9 ±0.2 ±0.4	0.3 ±0.2 ±0.7	1.2 ±0.3 ±0.8	3
$2e/\mu+ \geq 1\tau$, on-Z					
200	0.67 ±0.06 ±0.21	20.2 ±0.9 ±5.6	256 ±4 ±66	276 ±4 ±66	215
500	0.02 ±0.01 ±0.01	0.5 ±0.1 ±0.2	1.8 ±0.3 ±0.9	2.3 ±0.3 ±0.9	4
800	0.00 ±0.00 ±0.00	0.14 ±0.07 ±0.04	0.1 ±0.1 ±0.7	0.2 ±0.1 ±0.7	0

Table 6: Results for the $H_{\mathrm{T}}^{\mathrm{leptons}}$ signal regions. Results are presented in number of expected events as N ± (stat) ± (syst).

Min. $p_{\mathrm{T}}^{\ell} \geq$ [GeV]	$t\bar{t}+V(V)$	$VV(V)$	Reducible	Total	Observed
$\geq 3e/\mu$, off-Z					
50	2.2 ±0.1 ±0.7	25.4 ±0.7 ±5.7	3.0 ±0.9 ±0.7	30.6 ±1.2 ±5.8	22
100	0.12 ±0.02 ±0.04	1.64 ±0.15 ±0.32	0.28 ±0.27 ±0.69	2.04 ±0.31 ±0.76	2
150	0.02 ±0.01 ±0.01	0.31 ±0.06 ±0.09	$0\ ^{+0.69}_{-0}$	0.34 ±0.06 ±0.70	0
$2e/\mu+ \geq 1\tau$, off-Z					
50	0.32 ±0.04 ±0.10	1.9 ±0.1 ±0.4	22 ±1 ±6	24 ±1 ±6	24
100	0.01 ±0.00 ±0.00	0.09 ±0.02 ±0.03	0.4 ±0.1 ±0.7	0.5 ±0.1 ±0.7	1
150	0.00 ±0.00 ±0.00	0.01 ±0.00 ±0.00	0.03 ±0.02 ±0.71	0.04 ±0.02 ±0.71	0
$\geq 3e/\mu$, on-Z					
50	4.1 ±0.1 ±1.2	143 ±3 ±33	7.5 ±2.0 ±1.9	155 ±3 ±33	156
100	0.33 ±0.04 ±0.10	7.7 ±0.6 ±2.4	0.17 ±0.46 ±0.69	8.2 ±0.7 ±2.5	16
150	0.04 ±0.01 ±0.01	1.1 ±0.2 ±0.3	0.16 ±0.18 ±0.69	1.31 ±0.27 ±0.74	4
$2e/\mu+ \geq 1\tau$, on-Z					
50	0.20 ±0.03 ±0.07	7.9 ±0.6 ±2.0	79 ±2 ±21	88 ±2 ±21	51
100	0.00 ±0.00 ±0.00	0.68 ±0.20 ±0.20	1.1 ±0.2 ±0.8	1.8 ±0.3 ±0.8	2
150	0.00 ±0.00 ±0.00	0.08 ±0.08 ±0.02	0.03 ±0.03 ±0.71	0.10 ±0.08 ±0.71	0

Table 7: Results for the minimum p_{T}^{ℓ} signal regions. Results are presented in number of expected events as N ± (stat) ± (syst).

$E_{\mathrm{T}}^{\mathrm{miss}} \geq$ [GeV]	$t\bar{t}+V(V)$	$VV(V)$	Reducible	Total	Observed
$\geq 3e/\mu$, off-Z					
Inclusive	5.1 ±0.2 ±1.6	167 ±2 ±29	42 ±8 ±6	214 ±8 ±30	231
100	1.6 ±0.1 ±0.5	8.0 ±0.2 ±1.5	6.1 ±1.0 ±1.1	15.7 ±1.0 ±1.9	16
200	0.13 ±0.03 ±0.06	0.40 ±0.03 ±0.20	0.1 ±0.2 ±0.7	0.7 ±0.2 ±0.7	1
300	0.01 ±0.01 ±0.00	0.12 ±0.02 ±0.02	$0\ ^{+0.69}_{-0}$	0.14 ±0.02 ±0.69	0
$2e/\mu+ \geq 1\tau$, off-Z					
Inclusive	1.3 ±0.1 ±0.4	31 ±1 ±5	1090 ±10 ±270	1120 ±10 ±270	1069
100	0.32 ±0.04 ±0.10	1.8 ±0.1 ±0.4	24.3 ±1.3 ±6.1	26.4 ±1.3 ±6.1	32
200	0.03 ±0.01 ±0.01	0.12 ±0.02 ±0.02	0.4 ±0.2 ±0.7	0.6 ±0.2 ±0.7	0
300	0.01 ±0.01 ±0.00	0.01 ±0.00 ±0.00	0.1 ±0.1 ±0.7	0.1 ±0.1 ±0.7	0
$\geq 3e/\mu$, on-Z					
Inclusive	7.4 ±0.2 ±2.4	2560 ±10 ±420	246 ±33 ±41	2812 ±35 ±424	2899
100	2.1 ±0.1 ±0.6	106 ±2 ±15	4.4 ±1.1 ±0.8	112 ±2 ±15	95
200	0.19 ±0.03 ±0.06	8.6 ±0.4 ±1.2	0.24 ±0.31 ±0.69	9.0 ±0.5 ±1.4	5
300	0.02 ±0.01 ±0.01	1.7 ±0.2 ±0.4	$0\ ^{+0.69}_{-0}$	1.8 ±0.2 ±0.8	0
$2e/\mu+ \geq 1\tau$, on-Z					
Inclusive	0.5 ±0.1 ±0.2	133 ±3 ±24	16470 ±40 ±4120	16600 ±40 ±4120	14386
100	0.13 ±0.02 ±0.06	10 ±1 ±2	10 ±1 ±3	20 ±1 ±3	18
200	0.01 ±0.00 ±0.01	1.6 ±0.2 ±0.6	0.1 ±0.1 ±0.7	1.7 ±0.3 ±1.0	1
300	0.00 ±0.00 ±0.00	0.00 ±0.00 ±0.00	$0\ ^{+0.71}_{-0}$	0.00 ±0.00 ±0.71	0

Table 8: Results for the low-$H_{\mathrm{T}}^{\mathrm{jets}}$, $E_{\mathrm{T}}^{\mathrm{miss}}$ signal regions. Results are presented in number of expected events as N ± (stat) ± (syst).

$E_{\mathrm{T}}^{\mathrm{miss}} \geq$ [GeV]	$t\bar{t}+V(V)$	$VV(V)$	Reducible	Total	Observed
$\geq 3e/\mu$, off-Z					
Inclusive	6.1 ±0.2 ±1.9	25 ±1 ±11	14 ±2 ±2	45 ±2 ±11	49
100	2.54 ±0.11 ±0.80	4.2 ±0.3 ±2.6	5.0 ±1.0 ±0.7	12 ±1 ±3	11
200	0.37 ±0.04 ±0.12	1.0 ±0.2 ±0.8	0.6 ±0.2 ±0.7	2.0 ±0.3 ±1.1	0
300	0.08 ±0.02 ±0.03	0.12 ±0.04 ±0.09	0.2 ±0.1 ±0.7	0.4 ±0.1 ±0.7	0
$2e/\mu+ \geq 1\tau$, off-Z					
Inclusive	1.5 ±0.1 ±0.5	3.9 ±0.4 ±1.6	109 ±3 ±26	114 ±3 ±26	124
100	0.6 ±0.1 ±0.2	2.1 ±0.3 ±0.9	18 ±1 ±5	21 ±1 ±5	32
200	0.13 ±0.02 ±0.04	0.5 ±0.1 ±0.3	1.9 ±0.3 ±0.8	2.5 ±0.4 ±0.9	5
300	0.02 ±0.01 ±0.01	0.1 ±0.1 ±0.1	0.3 ±0.1 ±0.7	0.4 ±0.1 ±0.7	1
$\geq 3e/\mu$, on-Z					
Inclusive	21.1 ±0.3 ±6.4	218 ±4 ±89	24.4 ±4.8 ±4.1	264 ±6 ±90	300
100	6.0 ±0.2 ±1.8	39 ±2 ±19	1.7 ±0.6 ±0.7	47 ±2 ±20	44
200	1.0 ±0.1 ±0.3	9 ±1 ±5	0.2 ±0.4 ±0.7	10 ±1 ±5	13
300	0.12 ±0.02 ±0.04	2.3 ±0.4 ±1.5	$0\ ^{+0.69}_{-0}$	2.4 ±0.4 ±1.7	1
$2e/\mu+ \geq 1\tau$, on-Z					
Inclusive	1.5 ±0.1 ±0.5	15 ±1 ±7	380 ±10 ±100	400 ±10 ±100	347
100	0.5 ±0.1 ±0.2	4.8 ±0.5 ±2.1	6.0 ±0.6 ±1.6	11 ±1 ±3	15
200	0.10 ±0.02 ±0.03	0.8 ±0.2 ±0.8	0.3 ±0.2 ±0.7	1.3 ±0.3 ±1.1	3
300	0.03 ±0.01 ±0.01	0.35 ±0.14 ±0.20	$0\ ^{+0.71}_{-0}$	0.37 ±0.14 ±0.73	1

Table 9: Results for the high-$H_{\mathrm{T}}^{\mathrm{jets}}$, $E_{\mathrm{T}}^{\mathrm{miss}}$ signal regions. Results are presented in number of expected events as N ± (stat) ± (syst).

$m_{\text{eff}} \geq$ [GeV]	$t\bar{t} + V(V)$	$VV(V)$	Reducible	Total	Observed
$\geq 3e/\mu$, off-Z					
600	2.8 ±0.1 ±0.9	11 ±1 ±6	4.2 ±1.1 ±0.7	18 ±1 ±6	15
1000	0.40 ±0.04 ±0.12	1.77 ±0.21 ±1.64	0.79 ±0.34 ±0.69	2.96 ±0.41 ±1.78	0
1500	0.05 ±0.02 ±0.02	0.54 ±0.19 ±0.79	0.02 ±0.01 ±0.69	0.60 ±0.19 ±1.05	0
$2e/\mu+ \geq 1\tau$, off-Z					
600	0.6 ±0.1 ±0.2	1.6 ±0.2 ±0.8	21 ±1 ±5	24 ±1 ±5	27
1000	0.06 ±0.02 ±0.02	0.2 ±0.1 ±0.2	1.2 ±0.3 ±0.8	1.4 ±0.4 ±0.8	4
1500	0.00 ±0.00 ±0.01	0.00 ±0.00 ±0.00	0.08 ±0.08 ±0.71	0.08 ±0.08 ±0.71	1
$\geq 3e/\mu$, on-Z					
600	8.9 ±0.2 ±2.7	79 ±2 ±43	10 ±3 ±2	98 ±4 ±43	94
1000	1.4 ±0.1 ±0.4	11 ±1 ±10	1.2 ±0.8 ±0.7	13 ±1 ±11	17
1500	0.11 ±0.02 ±0.06	1.82 ±0.34 ±2.72	0.15 ±0.18 ±0.69	2.09 ±0.38 ±2.81	1
$2e/\mu+ \geq 1\tau$, on-Z					
600	0.6 ±0.1 ±0.2	6.5 ±0.6 ±3.3	41 ±2 ±11	48 ±2 ±11	44
1000	0.05 ±0.02 ±0.02	0.8 ±0.2 ±0.6	3.0 ±0.5 ±1.1	3.9 ±0.5 ±1.2	4
1500	0.01 ±0.01 ±0.01	0.00 ±0.00 ±0.00	0.05 ±0.05 ±0.71	0.06 ±0.05 ±0.71	0

Table 10: Results for the m_{eff} signal regions. Results are presented in number of expected events as N ± (stat) ± (syst).

$m_{\text{eff}} \geq$ [GeV]	$t\bar{t} + V(V)$	$VV(V)$	Reducible	Total	Observed
$\geq 3e/\mu$, off-Z					
Inclusive	4.1 ±0.1 ±1.3	12.2 ±0.3 ±4.0	11.1 ±1.4 ±1.6	27.4 ±1.4 ±4.5	27
600	1.8 ±0.1 ±0.5	4.1 ±0.2 ±2.4	1.8 ±0.4 ±0.7	7.6 ±0.5 ±2.6	7
1000	0.32 ±0.04 ±0.10	1.1 ±0.2 ±1.2	0.5 ±0.3 ±0.7	1.9 ±0.3 ±1.4	0
1200	0.16 ±0.03 ±0.05	0.9 ±0.2 ±1.0	0.1 ±0.1 ±0.7	1.2 ±0.2 ±1.3	0
1500	0.04 ±0.01 ±0.02	0.6 ±0.2 ±0.8	0.01 ±0.01 ±0.69	0.6 ±0.2 ±1.1	0
$2e/\mu+ \geq 1\tau$, off-Z					
Inclusive	0.9 ±0.1 ±0.3	3.9 ±0.2 ±1.2	43 ±2 ±11	48 ±2 ±11	64
600	0.4 ±0.1 ±0.1	1.0 ±0.1 ±0.5	7 ±1 ±2	8 ±1 ±2	12
1000	0.04 ±0.01 ±0.02	0.1 ±0.1 ±0.1	0.6 ±0.3 ±0.7	0.8 ±0.3 ±0.7	4
1200	0.01 ±0.01 ±0.01	0.00 ±0.00 ±0.05	0.23 ±0.13 ±0.71	0.24 ±0.13 ±0.71	2
1500	0.00 ±0.00 ±0.01	0.00 ±0.00 ±0.00	0.04 ±0.06 ±0.71	0.04 ±0.06 ±0.71	1
$\geq 3e/\mu$, on-Z					
Inclusive	8.0 ±0.2 ±2.4	145 ±2 ±34	6 ±1 ±1	159 ±3 ±34	139
600	3.90 ±0.14 ±1.22	30.1 ±1.0 ±15.1	0.86 ±0.50 ±0.69	35 ±1 ±15	31
1000	0.84 ±0.1 ±0.3	5.4 ±0.5 ±5.0	$0\ ^{+0.69}_{-0}$	6 ±1 ±5	5
1200	0.4 ±0.1 ±0.q1	2.7 ±0.4 ±3.0	$0\ ^{+0.69}_{-0}$	3.0 ±0.4 ±3.1	0
1500	0.08 ±0.02 ±0.04	0.8 ±0.2 ±1.1	$0\ ^{+0.69}_{-0}$	0.9 ±0.2 ±1.3	0
$2e/\mu+ \geq 1\tau$, on-Z					
Inclusive	0.6 ±0.1 ±0.2	14.7 ±0.8 ±3.8	16 ±1 ±4	31.6 ±1.4 ±5.7	33
600	0.28 ±0.04 ±0.09	3.7 ±0.4 ±1.8	2.1 ±0.4 ±0.9	6.0 ±0.6 ±2.0	9
1000	0.03 ±0.01 ±0.01	0.6 ±0.2 ±0.4	0.3 ±0.2 ±0.7	0.9 ±0.2 ±0.8	0
1200	0.03 ±0.01 ±0.01	0.2 ±0.1 ±0.1	0.1 ±0.1 ±0.7	0.3 ±0.1 ±0.7	0
1500	0.0 ±0.0 ±0.0	0.0 ±0.0 ±0.0	$0\ ^{+0.71}_{-0}$	0.0 ±0.0 ±0.7	0

Table 11: Results for the high-$E_{\text{T}}^{\text{miss}}$, m_{eff} signal regions. Results are presented in number of expected events as N ± (stat) ± (syst).

$m_{\text{eff}} \geq$ [GeV]	$t\bar{t} + V(V)$	$VV(V)$	Reducible	Total	Observed
$\geq 3e/\mu$, on-Z					
Inclusive	6.1 ±0.2 ±1.9	192 ±3 ±40	12.2 ±2.2 ±1.9	210 ±3 ±41	180
600	2.1 ±0.1 ±0.6	13 ±1 ±7	2.8 ±1.4 ±0.8	18 ±2 ±7	17
1200	0.14 ±0.03 ±0.05	1.1 ±0.2 ±1.1	0.2 ±0.2 ±0.7	1.4 ±0.3 ±1.3	1
$2e/\mu+ \geq 1\tau$, on-Z					
Inclusive	0.3 ±0.1 ±0.1	3.4 ±0.2 ±0.9	32 ±1 ±8	36 ±1 ±8	41
600	0.07 ±0.02 ±0.03	0.5 ±0.1 ±0.5	1.8 ±0.3 ±0.9	2.3 ±0.3 ±1.0	4
1200	0.00 ±0.00 ±0.00	0.08 ±0.08 ±0.08	0.04 ±0.03 ±0.71	0.12 ±0.09 ±0.71	0

Table 12: Results for the high-m_{T}^{W}, m_{eff} signal regions. Results are presented in number of expected events as N ± (stat) ± (syst).

b-tags $\geq$	$t\bar{t} + V(V)$	$VV(V)$	Reducible	Total	Observed
$\geq 3e/\mu$, off-Z					
1	8.7 ±0.2 ±2.7	6.7 ±0.6 ±2.0	24.8 ±2.0 ±1.3	40 ±2 ±4	42
2	3.0 ±0.1 ±1.0	0.2 ±0.1 ±0.1	3.4 ±1.0 ±0.7	6.6 ±1.0 ±1.2	8
$2e/\mu+ \geq 1\tau$, off-Z					
1	2.0 ±0.1 ±0.6	0.7 ±0.1 ±0.2	127 ±3 ±31	130 ±3 ±31	158
2	0.8 ±0.1 ±0.3	0.00 ±0.00 ±0.00	28 ±2 ±7	29 ±2 ±7	41
$\geq 3e/\mu$, on-Z					
1	21.8 ±0.3 ±6.8	69 ±2 ±20	31 ±4 ±2	121 ±4 ±22	127
2	8.2 ±0.2 ±2.6	2.1 ±0.3 ±1.0	1.8 ±0.8 ±0.7	12 ±1 ±3	11
$2e/\mu+ \geq 1\tau$, on-Z					
1	1.5 ±0.1 ±0.5	5.4 ±0.5 ±1.7	146 ±3 ±37	153 ±3 ±37	229
2	0.5 ±0.1 ±0.2	0.1 ±0.1 ±0.1	12 ±1 ±3	13 ±1 ±3	13

Table 13: Results for the b-tag signal regions. Results are presented in number of expected events as N ± (stat) ± (syst).

$H_{\mathrm{T}}^{\mathrm{leptons}}$[GeV]	Observed	Expected	$^{+1\sigma}_{-1\sigma}$	$^{+2\sigma}_{-2\sigma}$
$\geq 3(e,\mu)$, off-Z				
Inclusive	5.4	4.7	$^{1.7}_{1.3}$	$^{3.8}_{2.1}$
≥ 200	1.2	1.6	$^{0.6}_{0.42}$	$^{1.4}_{0.71}$
≥ 500	0.37	0.41	$^{0.18}_{0.13}$	$^{0.34}_{0.14}$
≥ 800	0.21	0.22	$^{0.068}_{0.041}$	$^{0.26}_{0.059}$
$2(e,\mu)+\geq 1(\tau)$, off-Z				
Inclusive	24	25	$^{7.9}_{6.1}$	$^{17}_{11}$
≥ 200	2.8	2.9	$^{0.99}_{0.74}$	$^{2.2}_{1.2}$
≥ 500	0.2	0.25	$^{0.15}_{0.042}$	$^{0.36}_{0.092}$
≥ 800	0.23	0.25	$^{0.14}_{0.042}$	$^{0.32}_{0.095}$
$\geq 3(e,\mu)$, on-Z				
Inclusive	54	50	$^{17}_{13}$	$^{37}_{22}$
≥ 200	8.8	9.1	$^{2.9}_{2.2}$	$^{6.2}_{3.8}$
≥ 500	0.9	0.89	$^{0.31}_{0.27}$	$^{0.57}_{0.44}$
≥ 800	0.43	0.34	$^{0.16}_{0.06}$	$^{0.26}_{0.12}$
$2(e,\mu)+\geq 1(\tau)$, on-Z				
Inclusive	280	320	$^{97}_{77}$	$^{210}_{130}$
≥ 200	3.9	4.9	$^{1.6}_{1.2}$	$^{3.5}_{2}$
≥ 500	0.5	0.37	$^{0.16}_{0.093}$	$^{0.21}_{0.12}$
≥ 800	0.22	0.23	$^{0.056}_{0.039}$	$^{0.21}_{0.095}$

Table 14: Limits in the $H_{\mathrm{T}}^{\mathrm{leptons}}$ bins shown as the upper limit on number of new physics events per inverse femtobarn ($N_{95}/\int Ldt$).

B Tables of expected and observed limits

$E_{\mathrm{T}}^{\mathrm{miss}}$[GeV]	Observed	Expected	$^{+1\sigma}_{-1\sigma}$	$^{+2\sigma}_{-2\sigma}$
$\geq 3(e,\mu)$, off-Z				
Inclusive	5.4	4.7	$^{1.7}_{1.3}$	$^{3.8}_{2.1}$
≥ 50	0.78	0.98	$^{0.42}_{0.19}$	$^{0.82}_{0.39}$
≥ 100	0.38	0.34	$^{0.15}_{0.075}$	$^{0.39}_{0.096}$
≥ 150	0.21	0.23	$^{0.064}_{0.03}$	$^{0.23}_{0.057}$
$2(e,\mu)+\geq 1(\tau)$, off-Z				
Inclusive	24	25	$^{7.9}_{6.1}$	$^{17}_{11}$
≥ 50	1	1	$^{0.39}_{0.27}$	$^{0.91}_{0.37}$
≥ 100	0.32	0.26	$^{0.08}_{0.0096}$	$^{0.3}_{0.042}$
≥ 150	0.23	0.23	$^{0.022}_{0.011}$	$^{0.17}_{0.046}$
$\geq 3(e,\mu)$, on-Z				
Inclusive	54	50	$^{17}_{13}$	$^{37}_{22}$
≥ 50	3.5	3.4	$^{1.2}_{0.84}$	$^{2.7}_{1.5}$
≥ 100	1.2	0.83	$^{0.41}_{0.12}$	$^{1.4}_{0.26}$
≥ 150	0.51	0.29	$^{0.12}_{0.068}$	$^{0.34}_{0.1}$
$2(e,\mu)+\geq 1(\tau)$, on-Z				
Inclusive	280	320	$^{97}_{77}$	$^{210}_{130}$
≥ 50	0.89	1.5	$^{0.54}_{0.39}$	$^{1.2}_{0.64}$
≥ 100	0.34	0.3	$^{0.16}_{0.044}$	$^{0.27}_{0.092}$
≥ 150	0.25	0.25	$^{0.0077}_{0.036}$	$^{0.071}_{0.06}$

Table 15: Limits in the Min. p_{T}^{ℓ} bins shown as the upper limit on number of new physics events per inverse femtobarn ($N_{95}/\int Ldt$).

$E_{\mathrm{T}}^{\mathrm{miss}}$[GeV]	Observed	Expected	$^{+1\sigma}{}_{-1\sigma}$	$^{+2\sigma}{}_{-2\sigma}$
$\geq 3(e,\mu)$, off-Z				
Inclusive	4.2	3.6	$^{1.4}{}_{0.98}$	$^{3.1}{}_{1.6}$
≥ 100	0.79	0.73	$^{0.35}{}_{0.13}$	$^{0.78}{}_{0.29}$
≥ 200	0.28	0.24	$^{0.12}{}_{0.023}$	$^{0.32}{}_{0.089}$
≥ 300	0.21	0.21	$^{0.028}{}_{0.03}$	$^{0.2}{}_{0.079}$
$2(e,\mu)+\geq 1(\tau)$, off-Z				
Inclusive	22	23	$^{7}{}_{5.5}$	$^{15}{}_{9.6}$
≥ 100	1.3	1.2	$^{0.38}{}_{0.33}$	$^{1.1}{}_{0.5}$
≥ 200	0.21	0.22	$^{0.093}{}_{0.026}$	$^{0.29}{}_{0.069}$
≥ 300	0.22	0.23	$^{0.029}{}_{0.015}$	$^{0.15}{}_{0.065}$
$\geq 3(e,\mu)$, on-Z				
Inclusive	44	41	$^{15}{}_{11}$	$^{32}{}_{18}$
≥ 100	1.3	1.7	$^{0.7}{}_{0.47}$	$^{1.6}{}_{0.79}$
≥ 200	0.47	0.51	$^{0.32}{}_{0.12}$	$^{0.61}{}_{0.24}$
≥ 300	0.23	0.26	$^{0.17}{}_{0.037}$	$^{0.33}{}_{0.094}$
$2(e,\mu)+\geq 1(\tau)$, on-Z				
Inclusive	300	320	$^{98}{}_{74}$	$^{200}{}_{120}$
≥ 100	0.89	0.89	$^{0.38}{}_{0.23}$	$^{0.89}{}_{0.45}$
≥ 200	0.29	0.31	$^{0.14}{}_{0.061}$	$^{0.28}{}_{0.11}$
≥ 300	0.2	0.21	$^{0.0093}{}_{0.028}$	$^{0.068}{}_{0.057}$

Table 16: Limits in the $E_{\mathrm{T}}^{\mathrm{miss}}$ bins with $H_{\mathrm{T}}^{\mathrm{jets}} \leq 100$ GeV requirement shown as the upper limit on number of new physics events per inverse femtobarn ($N_{95}/\int Ldt$).

$E_{\mathrm{T}}^{\mathrm{miss}}$[GeV]	Observed	Expected	$^{+1\sigma}{}_{-1\sigma}$	$^{+2\sigma}{}_{-2\sigma}$
$\geq 3(e,\mu)$, off-Z				
Inclusive	1.9	1.7	$^{0.65}{}_{0.27}$	$^{1.5}{}_{0.52}$
≥ 100	0.71	0.71	$^{0.26}{}_{0.2}$	$^{0.54}{}_{0.37}$
≥ 200	0.22	0.26	$^{0.15}{}_{0.038}$	$^{0.3}{}_{0.1}$
≥ 300	0.22	0.21	$^{0.062}{}_{0.026}$	$^{0.26}{}_{0.086}$
$2(e,\mu)+\geq 1(\tau)$, off-Z				
Inclusive	3.1	2.8	$^{0.99}{}_{0.72}$	$^{2.2}{}_{1.2}$
≥ 100	1.5	0.96	$^{0.42}{}_{0.2}$	$^{1.1}{}_{0.31}$
≥ 200	0.53	0.39	$^{0.14}{}_{0.087}$	$^{0.37}{}_{0.16}$
≥ 300	0.28	0.24	$^{0.1}{}_{0.024}$	$^{0.3}{}_{0.04}$
$\geq 3(e,\mu)$, on-Z				
Inclusive	9.7	8.8	$^{2.5}{}_{2}$	$^{5.3}{}_{3.6}$
≥ 100	2	2	$^{0.61}{}_{0.28}$	$^{1.5}{}_{0.49}$
≥ 200	0.99	0.78	$^{0.23}{}_{0.096}$	$^{0.32}{}_{0.17}$
≥ 300	0.29	0.3	$^{0.19}{}_{0.086}$	$^{0.29}{}_{0.12}$
$2(e,\mu)+\geq 1(\tau)$, on-Z				
Inclusive	6.8	7.8	$^{2.5}{}_{1.9}$	$^{5.4}{}_{3.2}$
≥ 100	0.9	0.74	$^{0.34}{}_{0.19}$	$^{0.54}{}_{0.3}$
≥ 200	0.44	0.33	$^{0.2}{}_{0.069}$	$^{0.35}{}_{0.15}$
≥ 300	0.29	0.28	$^{0.028}{}_{0.079}$	$^{0.22}{}_{0.12}$

Table 17: Limits in the $E_{\mathrm{T}}^{\mathrm{miss}}$ bins with $H_{\mathrm{T}}^{\mathrm{jets}} \geq 100$ GeV requirement shown as the upper limit on number of new physics events per inverse femtobarn ($N_{95}/\int Ldt$).

m_{eff}[GeV]	Observed	Expected	$^{+1\sigma}_{-1\sigma}$	$^{+2\sigma}_{-2\sigma}$
$\geq 3(e,\mu)$, off-Z				
Inclusive	5.4	4.7	$^{1.7}_{1.3}$	$^{3.8}_{2.1}$
≥ 600	0.88	0.92	$^{0.33}_{0.16}$	$^{0.89}_{0.36}$
≥ 1000	0.19	0.24	$^{0.15}_{0.059}$	$^{0.39}_{0.088}$
≥ 1500	0.2	0.25	$^{0.076}_{0.052}$	$^{0.29}_{0.11}$
$2(e,\mu)+\geq 1(\tau)$, off-Z				
Inclusive	24	25	$^{7.9}_{6.1}$	$^{17}_{11}$
≥ 600	1.1	0.96	$^{0.4}_{0.23}$	$^{1}_{0.34}$
≥ 1000	0.51	0.37	$^{0.14}_{0.062}$	$^{0.39}_{0.12}$
≥ 1500	0.25	0.22	$^{0.062}_{0.035}$	$^{0.16}_{0.061}$
$\geq 3(e,\mu)$, on-Z				
Inclusive	54	50	$^{17}_{13}$	$^{37}_{22}$
≥ 600	3.7	3.8	$^{0.73}_{0.69}$	$^{1.8}_{1.3}$
≥ 1000	1.4	1.3	$^{0.33}_{0.21}$	$^{0.45}_{0.36}$
≥ 1500	0.29	0.33	$^{0.16}_{0.046}$	$^{0.29}_{0.13}$
$2(e,\mu)+\geq 1(\tau)$, on-Z				
Inclusive	280	320	$^{97}_{77}$	$^{210}_{130}$
≥ 600	1.5	1.5	$^{0.58}_{0.22}$	$^{1.2}_{0.55}$
≥ 1000	0.46	0.41	$^{0.18}_{0.099}$	$^{0.44}_{0.13}$
≥ 1500	0.19	0.25	$^{0}_{0.061}$	$^{0.086}_{0.094}$

Table 18: Limits in the m_{eff} bins shown as the upper limit on number of new physics events per inverse femtobarn ($N_{95}/\int Ldt$).

m_{eff}[GeV]	Observed	Expected	$^{+1\sigma}_{-1\sigma}$	$^{+2\sigma}_{-2\sigma}$
$\geq 3(e,\mu)$, off-Z				
Inclusive	1	1	$^{0.46}_{0.12}$	$^{1.1}_{0.38}$
≥ 600	0.58	0.57	$^{0.31}_{0.11}$	$^{0.53}_{0.18}$
≥ 1200	0.23	0.29	$^{0.14}_{0.097}$	$^{0.32}_{0.15}$
$2(e,\mu)+\geq 1(\tau)$, off-Z				
Inclusive	2.4	1.8	$^{0.54}_{0.55}$	$^{1.6}_{0.84}$
≥ 600	0.74	0.56	$^{0.31}_{0.13}$	$^{0.41}_{0.22}$
≥ 1200	0.4	0.3	$^{0.14}_{0.017}$	$^{0.31}_{0.077}$
$\geq 3(e,\mu)$, on-Z				
Inclusive	2.8	3.2	$^{1.1}_{0.82}$	$^{2.4}_{1.4}$
≥ 600	1.6	1.6	$^{0.52}_{0.23}$	$^{1.2}_{0.52}$
≥ 1200	0.21	0.34	$^{0.24}_{0.089}$	$^{0.4}_{0.18}$
$2(e,\mu)+\geq 1(\tau)$, on-Z				
Inclusive	1.2	1	$^{0.54}_{0.15}$	$^{1.1}_{0.34}$
≥ 600	0.74	0.54	$^{0.24}_{0.087}$	$^{0.36}_{0.14}$
≥ 1200	0.2	0.23	$^{0.046}_{0.045}$	$^{0.25}_{0.094}$

Table 19: Limits in the m_{eff} bins with $E_{\text{T}}^{\text{miss}} \geq 100$ GeV requirement shown as the upper limit on number of new physics events per inverse femtobarn ($N_{95}/\int Ldt$).

m_{eff}[GeV]	Observed	Expected	$^{+1\sigma}{}_{-1\sigma}$	$^{+2\sigma}{}_{-2\sigma}$
$\geq 3(e,\mu)$, on-Z				
Inclusive	3	3.6	$^{1.3}{}_{0.95}$	$^{2.8}{}_{1.6}$
≥ 600	0.98	0.97	$^{0.32}{}_{0.15}$	$^{0.83}{}_{0.17}$
≥ 1200	0.27	0.27	$^{0.16}{}_{0.021}$	$^{0.33}{}_{0.11}$
$2(e,\mu)+\geq 1(\tau)$, on-Z				
Inclusive	1.6	1.4	$^{0.43}{}_{0.37}$	$^{1.2}{}_{0.55}$
≥ 600	0.53	0.37	$^{0.19}{}_{0.054}$	$^{0.47}{}_{0.086}$
≥ 1200	0.21	0.22	$^{0.031}{}_{0.0085}$	$^{0.11}{}_{0.022}$

Table 20: Limits in the high-m_{T}^{W}, m_{eff} signal regions shown as the upper limit on number of new physics events per inverse femtobarn ($N_{95}/\int Ldt$).

m_{eff}[GeV]	Observed	Expected	$^{+1\sigma}{}_{-1\sigma}$	$^{+2\sigma}{}_{-2\sigma}$
$\geq 3(e,\mu)$, off-Z				
Inclusive	5.4	4.7	$^{1.7}{}_{1.3}$	$^{3.8}{}_{2.1}$
≥ 1	1.2	1.1	$^{0.57}{}_{0.29}$	$^{1.2}{}_{0.51}$
≥ 2	0.62	0.55	$^{0.19}{}_{0.18}$	$^{0.3}{}_{0.28}$
$2(e,\mu)+\geq 1(\tau)$, off-Z				
Inclusive	24	25	$^{7.9}{}_{6.1}$	$^{17}{}_{11}$
≥ 1	4.3	3.3	$^{1.2}{}_{0.92}$	$^{2.7}{}_{1.6}$
≥ 2	1.8	1.2	$^{0.52}{}_{0.3}$	$^{1.1}{}_{0.51}$
$\geq 3(e,\mu)$, on-Z				
Inclusive	54	50	$^{17}{}_{13}$	$^{38}{}_{22}$
≥ 1	3	2.8	$^{0.96}{}_{0.71}$	$^{2.1}{}_{1.2}$
≥ 2	0.7	0.7	$^{0.38}{}_{0.23}$	$^{0.61}{}_{0.31}$
$2(e,\mu)+\geq 1(\tau)$, on-Z				
Inclusive	340	360	$^{110}{}_{53}$	$^{200}{}_{1702}$
≥ 1	7.2	4.3	$^{1.8}{}_{1.1}$	$^{3.8}{}_{1.9}$
≥ 2	0.73	0.7	$^{0.32}{}_{0.12}$	$^{0.69}{}_{0.27}$

Table 21: Limits in the signal regions defined by the number of b-tags shown as the upper limit on number of new physics events per inverse femtobarn ($N_{95}/\int Ldt$).

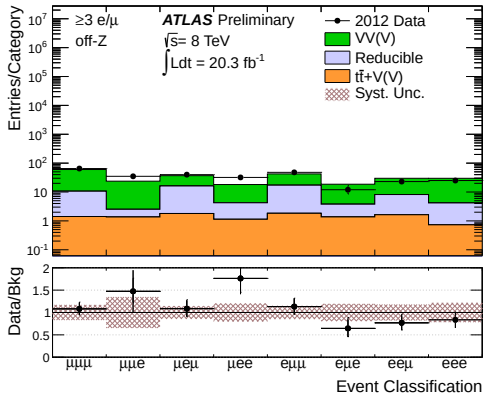

(a) Event Classification

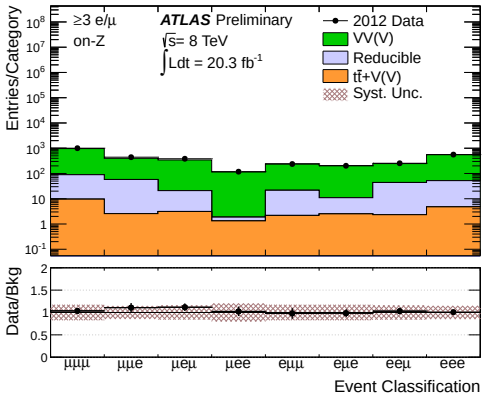

(b) Event Classification

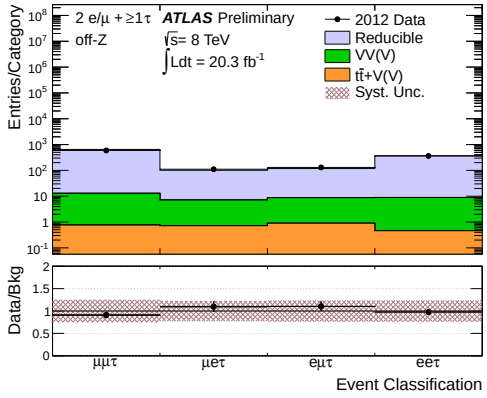

(c) Event Classification

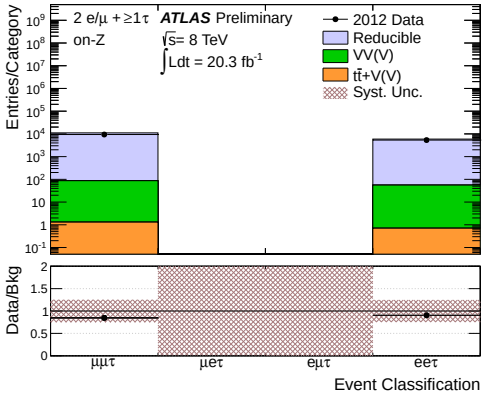

(d) Event Classification

Figure 18: The breakdown of the events by lepton flavor for predicted background and observation in the (a) off-Z, $\geq 3e/\mu$, (b) on-Z, $\geq 3e/\mu$, (c) off-Z, $2e/\mu+ \geq 1\tau_{\text{had}}$, and (d) on-$Z$, $2e/\mu+ \geq 1\tau_{\text{had}}$ channels.

C Additional public plots

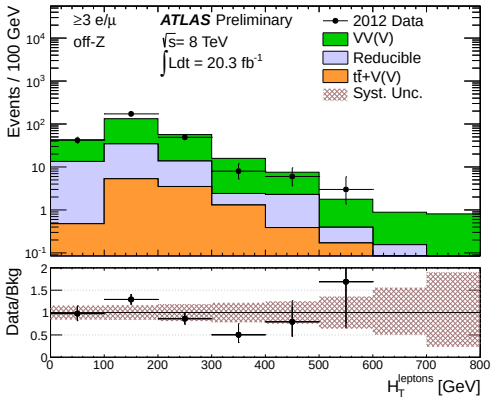

(a) $H_{\mathrm{T}}^{\mathrm{leptons}}$

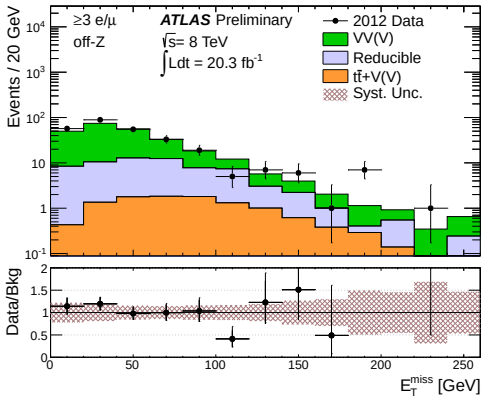

(b) $E_{\mathrm{T}}^{\mathrm{miss}}$

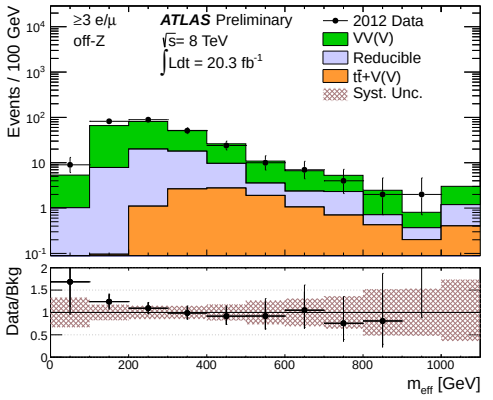

(c) m_{eff}

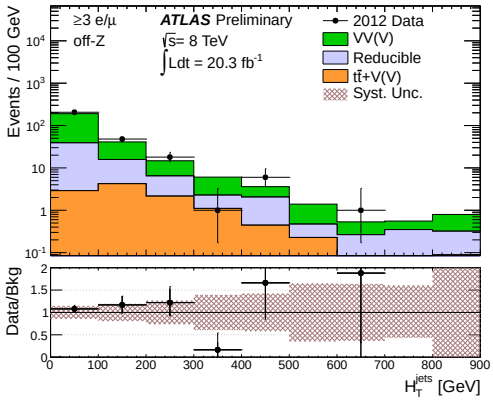

(d) $H_{\mathrm{T}}^{\mathrm{jets}}$

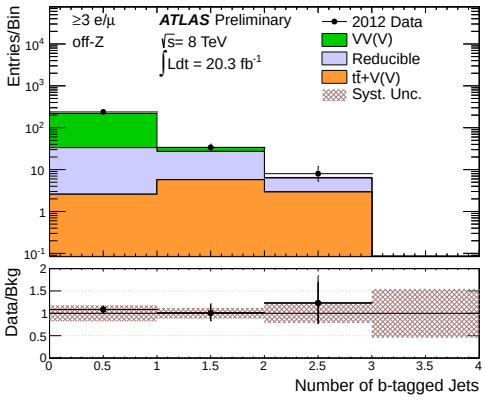

(e) Number of b-tagged Jets

Figure 19: Distributions of the different kinematic variables are shown in the off-Z, $\geq 3e/\mu$ channel. The background histograms are stacked. The last bin shows the overflows. The bottom panel shows the ratio of events observed in data to those expected from background sources for each bin.

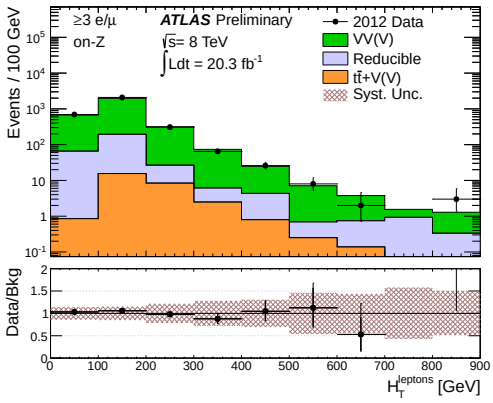

(a) $H_{\mathrm{T}}^{\mathrm{leptons}}$

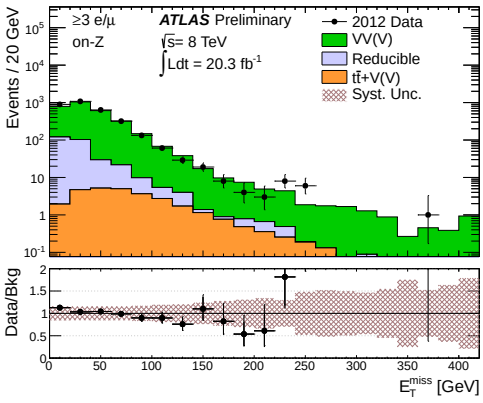

(b) $E_{\mathrm{T}}^{\mathrm{miss}}$

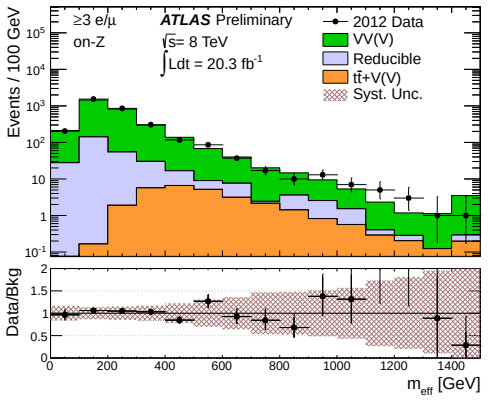

(c) m_{eff}

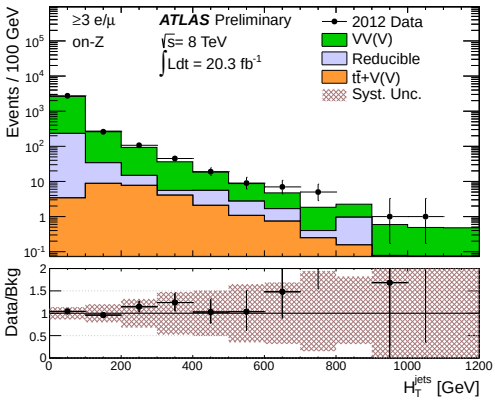

(d) $H_{\mathrm{T}}^{\mathrm{jets}}$

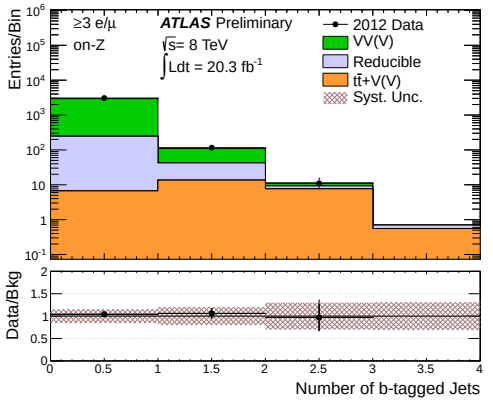

(e) Number of b-tagged Jets

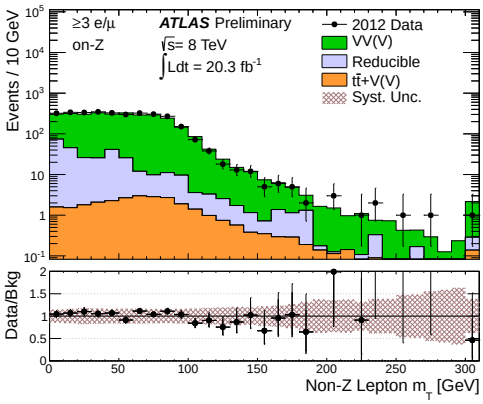

(f) m_{T}^{W}

Figure 20: Distributions of the different kinematic variables are shown in the on-Z, $\geq 3e/\mu$ channel. The background histograms are stacked. The last bin shows the overflows. The bottom panel shows the ratio of events observed in data to those expected from background sources for each bin.

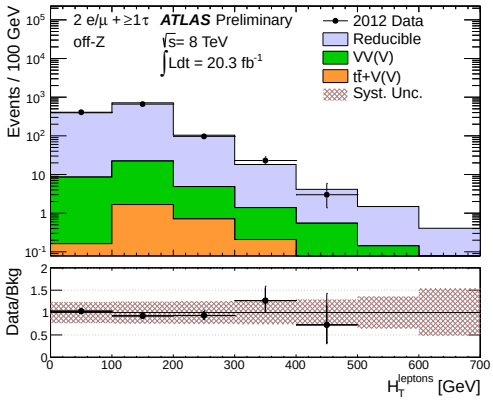

(a) $H_{\mathrm{T}}^{\mathrm{leptons}}$

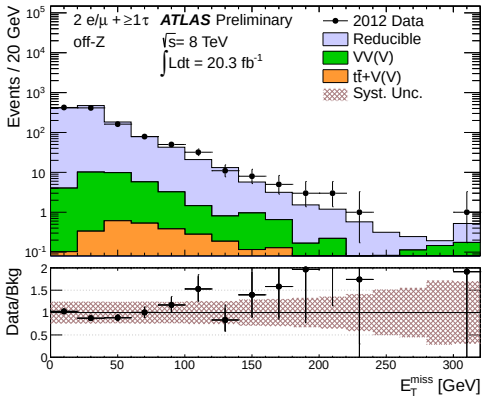

(b) $E_{\mathrm{T}}^{\mathrm{miss}}$

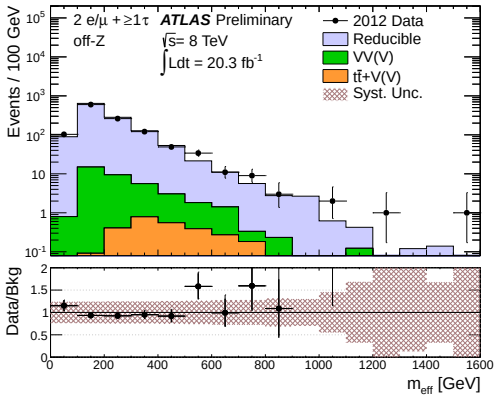

(c) m_{eff}

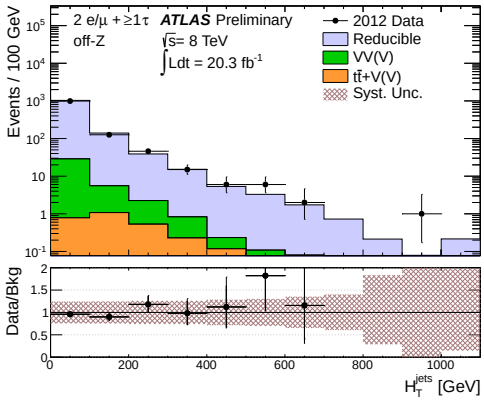

(d) $H_{\mathrm{T}}^{\mathrm{jets}}$

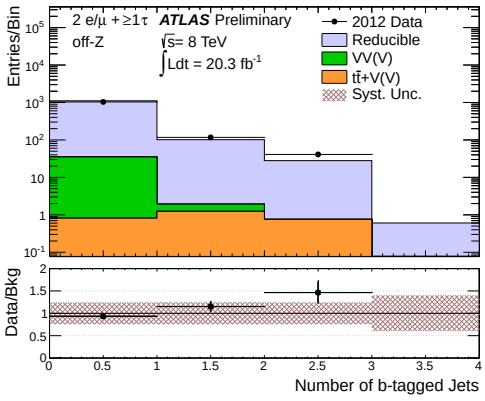

(e) Number of b-tagged Jets

Figure 21: Distributions of the different kinematic variables are shown in the off-Z, $2e/\mu+ \geq 1\tau_{\mathrm{had}}$ channel. The background histograms are stacked. The last bin shows the overflows. The bottom panel shows the ratio of events observed in data to those expected from background sources for each bin.

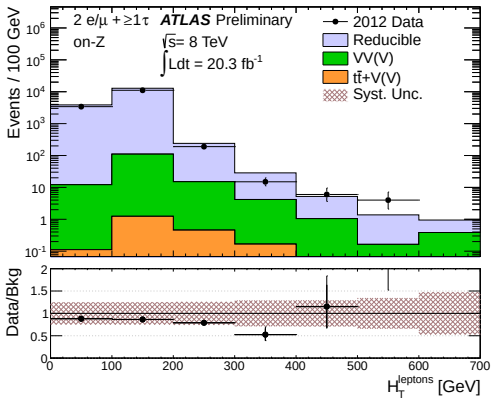

(a) $H_{\mathrm{T}}^{\mathrm{leptons}}$

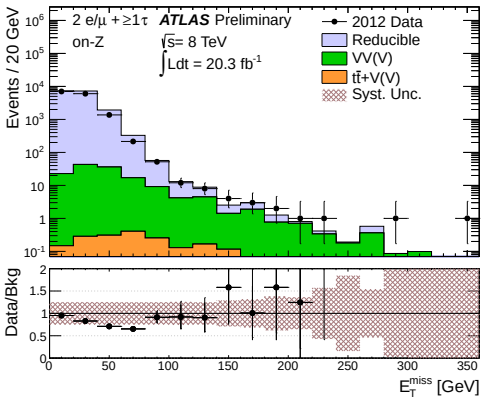

(b) $E_{\mathrm{T}}^{\mathrm{miss}}$

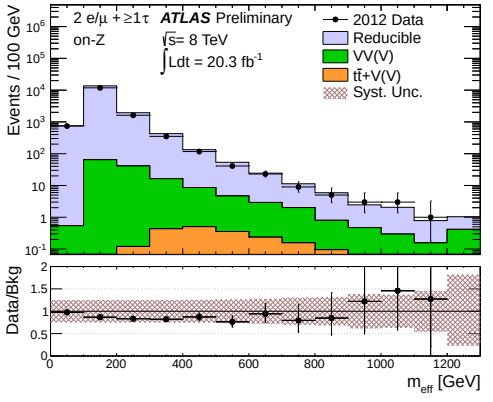

(c) m_{eff}

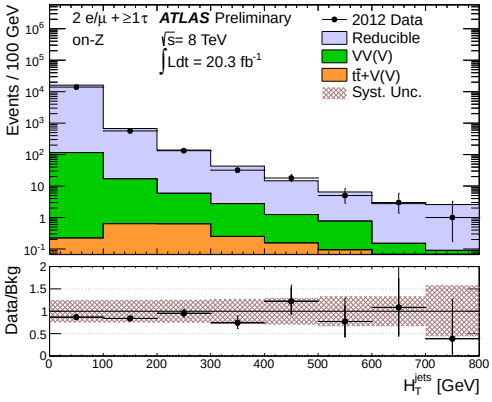

(d) $H_{\mathrm{T}}^{\mathrm{jets}}$

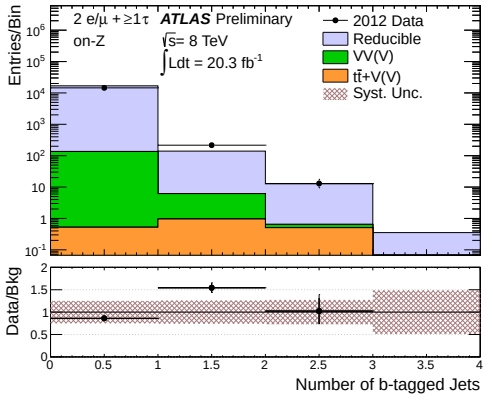

(e) Number of b-tagged Jets

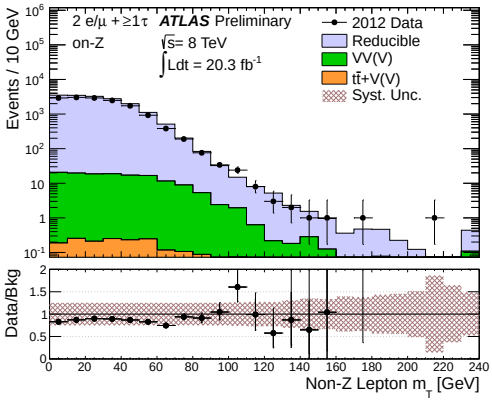

(f) m_{T}^{W}

Figure 22: Distributions of the different kinematic variables are shown in the on-Z, $2e/\mu+ \geq 1\tau_{\mathrm{had}}$ channel. The background histograms are stacked. The last bin shows the overflows. The bottom panel shows the ratio of events observed in data to those expected from background sources for each bin.

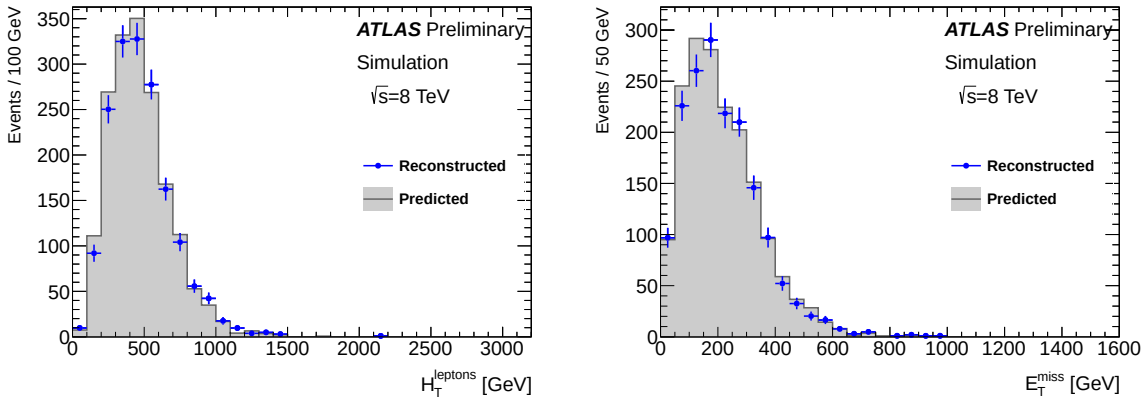

(a) $H_{\mathrm{T}}^{\mathrm{leptons}}$

(b) $E_{\mathrm{T}}^{\mathrm{miss}}$

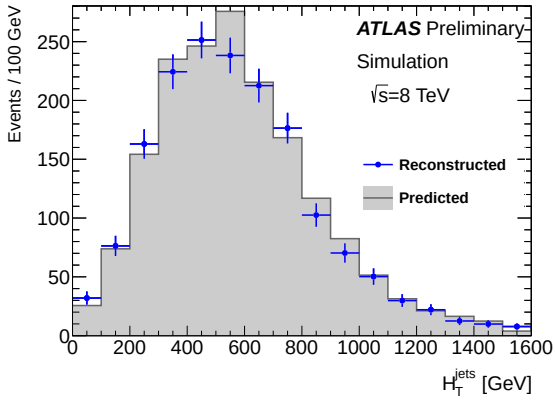

(c) $H_{\mathrm{T}}^{\mathrm{jets}}$

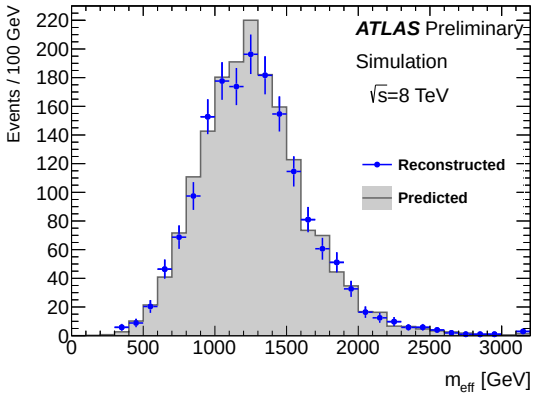

(d) m_{eff}

Figure 23: Figure shows the different kinematic distributions for the off-Z, $\geq 3e/\mu$ channel for the vector-like B quark model (see ATLAS-CONF-2013-056 for details) with m(B) = 800 GeV. The filled histogram is the prediction using fiducial selection and efficiencies, and the points are the reconstructed quantity.

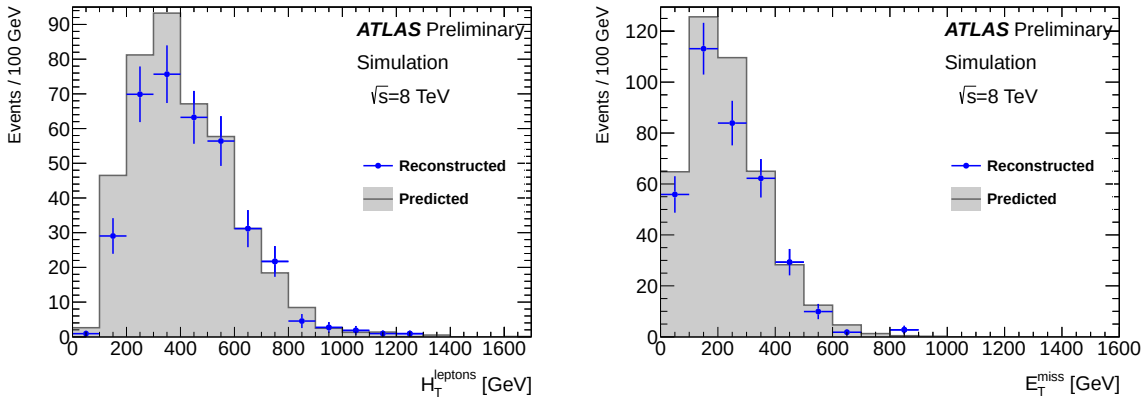

(a) $H_{\mathrm{T}}^{\mathrm{leptons}}$

(b) $E_{\mathrm{T}}^{\mathrm{miss}}$

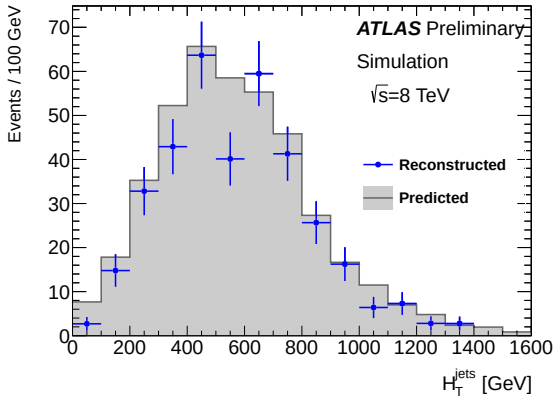

(c) $H_{\mathrm{T}}^{\mathrm{jets}}$

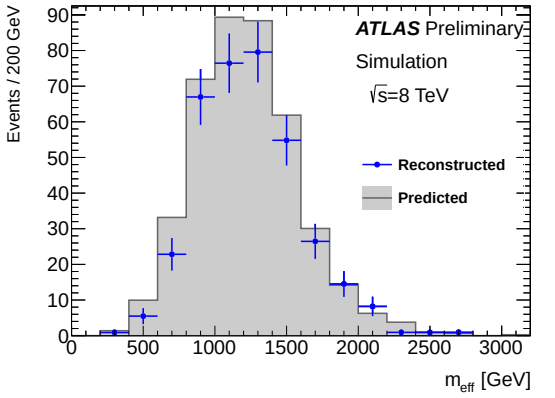

(d) m_{eff}

Figure 24: Figure shows the different kinematic distributions for the off-Z, $2e/\mu+ \geq 1\tau_{\mathrm{had}}$ channel for the vector-like B quark model (see ATLAS-CONF-2013-056 for details) with $m(\mathrm{B}) = 800$ GeV. The filled histogram is the prediction using fiducial selection and efficiencies, and the points are the reconstructed quantity.

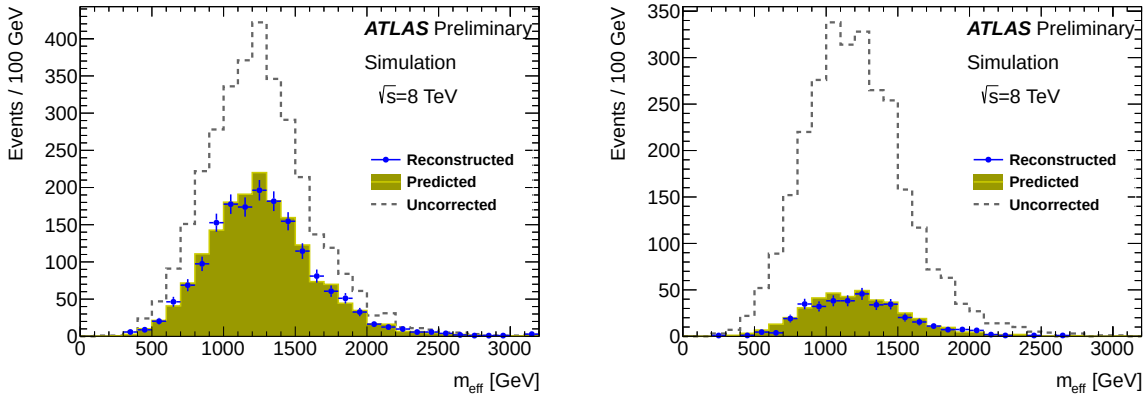

(a) d_4 (m = 800 GeV) m_{eff}, 3L

(b) d_4 (m = 800 GeV) m_{eff}, 2L+τ

Figure 25: Figure shows the m_{eff} distribution for (a) the off-Z, $\geq 3e/\mu$ channel (left) and (b) the off-Z, $2e/\mu+ \geq 1\tau_{\text{had}}$ channel for the vector-like B quark model (see ATLAS-CONF-2013-056 for details) model with m(B) = 800 GeV. The filled histogram is the prediction using fiducial selection and efficiencies, and the points are the reconstructed quantity. The dashed line (Uncorrected) shows the prediction without applying the fiducial efficiencies.